GREEN SYNTHESIS OF SILVER NANOWIRES AND NOVEL ASSEMBLY TECHNIQUE FOR IRON OXIDE NANOCUBES

A Thesis Submitted to
the Graduate School of Engineering and Sciences of
İzmir Institute of Technology
in Partial Fulfillment of the Requirements for the Degree of

DOCTOR OF PHILOSOPHY

in Materials Science and Engineering

by
Tuğçe Aybüke ARICA GÜVENÇ

November 2024
İZMİR

We approve the thesis of **Tuğçe Aybüke ARICA GÜVENÇ**

Examining Committee Members:

Prof. Dr. Sinan BALCI
Department of Photonics, IZTECH

Prof. Dr. Yaşar AKDOĞAN
Department of Materials Science and Engineering, IZTECH

Assoc. Prof. Dr. Engin KARABUDAK
Department of Chemistry, IZTECH

Assoc. Prof. Dr. Muhammed ÜÇÜNCÜ
Department of Pharmaceutical Basic Sciences, IKCU

Assoc. Prof. Dr. Burak GÜLTEKİN
Department of Energy, EU

8 November 2024

Prof. Dr. Sinan BALCI
Supervisor, Department of
Photonics, IZTECH

Assoc. Prof. Dr. Umut ADEM
Co-Supervisor, Material Science
and Engineering, IZTECH

Prof. Dr. Yaşar AKDOĞAN
Head of the Department of
Materials Science and Engineering

Prof. Dr. Mehtap EANES
Dean of the Graduate School

ACKNOWLEDGEMENTS

Firstly, I would like to thank my supervisor, Prof. Dr. Sinan Balcı, for his support and advice throughout the thesis. I am also thankful to Assist. Prof. Dr. Fadime Mert Balcı for her valuable advice and discussion.

I am grateful to Prof. Dr. Teresa Pellegrino for her guidance, valuable discussion, and understanding, as well as for introducing me to her valuable research groups, who are helpful and open to sharing ideas.

Also, I would like to thank Ecem Tiryaki, Ana Maria Panaite, Houman Bahmani Jalali, Güncem Özgün Eren, Stefano Toso, Irina Gushchina, Aleksandra Predeina, Pascal Rusch, Umberto Filippi, Alessandro Di Girolama, Nikolaos Livakas and Clara Otero Martinez for their friendship and support during my doctoral studies at IIT.

I want to thank Sema Sarısözen, Necip Ayhan Tertemiz, Zeynep Kahraman, Nahit Polat, Metin Tan and Levent Karacasulu for their valuable help and friendship support. I would also like to thank Ayhan Ece Şirin, who always gave me her friendly support and sincerely motivated me.

Thank you to my husband, Çetin Meriç Güvenç, for his sincere love and support throughout this journey. Finally, I am eternally grateful to my family for their endless encouragement and unconditional support.

I would like to express my gratitude for the support given by TÜBİTAK (The Scientific and Technological Research Council of Turkey) within the scope of 2214-A-International Research Scholarship Program during my doctoral study.

ABSTRACT

GREEN SYNTHESIS OF SILVER NANOWIRES AND NOVEL ASSEMBLY TECHNIQUE FOR IRON OXIDE NANOCUBES

Silver nanowires are known for their excellent electrical conductivity, plasmonic behavior, and flexibility, making them highly suitable for various advanced applications. This thesis investigated the dual role of silver nanowires as both a target for environmentally friendly synthesis approaches and a template for improved magnetic nanostructures in biomedical applications. The first part of the study explored the influence of transition metal salts in controlling the morphology of silver nanowires. Employing the eco-friendly reducing agent as glycerol demonstrated that specific transition metal salts can significantly impact the nanowire morphology. Through careful optimization of experimental conditions, silver nanowires were successfully synthesized with high aspect ratios. This green synthesis approach provides a sustainable route to producing nanowires for applications in flexible electronics, sensors, and beyond. In the second part, silver nanowires were presented as a high-surface-area template to enhance the magnetic hyperthermia performance of iron oxide nanocubes. Iron oxide nanocubes were assembled on silver nanowires' surface to increase their magnetic anisotropy. Magnetic characterization and specific absorption rate analysis reveal that this structure improves the heating efficiency under alternating magnetic fields depending on the applied magnetic field conditions and outperforms individual iron oxide nanoparticles.

ÖZET

GÜMÜŞ NANOTELLERİN YEŞİL SENTEZİ VE DEMİR OKSİT NANOKÜPLER İÇİN YENİ BİR DİZİLİM TEKNİĞİ

Gümüş nanoteller, mükemmel elektriksel iletkenlikleri, plazmonik davranışları ve esneklikleriyle bilinir ve bu nedenle çeşitli gelişmiş uygulamalar için oldukça uygundurlar. Bu tez çalışması, gümüş nanotellerin hem çevre dostu sentezini, hem de biyomedikal uygulamalarda gelişmiş manyetik nanoyapılar için bir şablon olarak ikili rolünü araştırmıştır. Çalışmanın ilk bölümünde, geçiş metali tuzlarının gümüş nanotellerin morfolojisini kontrol etmedeki etkisi araştırılmıştır. Çevre dostu indirgeyici madde olarak gliserolün kullanılması, belirli geçiş metali tuzlarının nanotel morfolojisini önemli ölçüde etkileyebileceğini göstermiştir. Deneysel koşulların dikkatli bir şekilde optimize edilmesiyle, gümüş nanoteller yüksek en boy oranlarıyla başarıyla sentezlenmiştir. Bu yeşil sentez yaklaşımı, esnek elektronik, sensörler ve daha fazlası için nanoteller üretmek için sürdürülebilir bir yol sağlar. İkinci bölümde, gümüş nanoteller, demir oksit nanoküplerin manyetik hipertermi performansını artırmak için yüksek yüzey alanlı bir şablon olarak sunulmuştur. Demir oksit nanoküpler, manyetik anizotropilerini artırmak için gümüş nanotellerin yüzeyine dekore edilmiştir. Manyetik karakterizasyon ve özgül emilim oranı analizi, bu yapının uygulanan manyetik alan koşullarına bağlı olarak değişen manyetik alanlar altında ısıtma verimliliğini artırdığını ve tek başına demir oksit nanopartiküllerinden daha üstün performans gösterdiğini ortaya koymaktadır.

TABLE OF CONTENTS

LIST OF FIGURES

LIST OF TABLES

ABBREVIATIONS

AgNWs	Silver Nanowires
ATR-FTIR	Attenuated Total Reflectance-Fourier Transform Infrared
DLS	Dynamic light scattering
ICP-OES	Inductively Coupled Plasma-Optical Emission Spectrometry
IONCs	Iron Oxide Nanocubes
MHT	Magnetic Hyperthermia Therapy
MTP	Multiple Twinned Particles
PEI	Polyethyleneimine
PVP	Polyvinylpyrrolidone
SEM	Scanning Electron Microscopy
SPIONs	Superparamagnetic Iron Oxide Nanoparticles
TEM	Transmission Electron Microscopy
UV-Vis	Ultraviolet-Visible
XRD	X-ray Diffraction

CHAPTER 1

INTRODUCTION

1.1. Overview

Nanotechnology is the field of science and technology that involves synthesizing and processing materials at the nanoscale to produce cutting-edge materials and devices. This technology is based chiefly on nanostructures with at least one dimension ranging from 1 to 100 nm. Nanostructures confine electrons due to their high specific surface area to volume ratio and exhibit superior electronic, optical, and magnetic properties than their bulk counterparts. The most important features of these structures that cannot be achieved in bulk counterparts are localized surface plasmon resonance and superparamagnetism.

Silver nanowires (AgNWs) have gained significant attention in the past decade due to their exceptional electrical, optical, and mechanical properties. These properties make them promising candidates for a wide variety of advanced applications. AgNWs often exhibit high electrical conductivity, plasmonic behavior, and flexibility, with diameters typically ranging from 10 to 100 nanometers and lengths reaching several tens of micrometers. These characteristics make them suitable for use in research areas such as transparent conductors, flexible electronics, sensors, and photonic devices. Polyol synthesis is a widely used method for synthesizing AgNWs since it is simple and easy to scale.[1] However, new methods for more sustainable and green synthesis are being investigated to reduce the negative environmental impacts of toxic reagents such as ethylene glycol, often used in polyol synthesis. These approaches often use plant extracts, microorganisms, or other environmentally friendly reductants. In addition, the aspect ratio of AgNWs is decisive for the applications in which they will be used. The effects of silver source, surfactant, precursor molar ratio, and temperature parameters, as well as transition metal salts on morphology are being actively investigated.[2] AgNWs are also being investigated in developing hybrid nanostructures, which serve as templates for other nanomaterials.[3] For example, combining silver nanowires with iron oxide nanoparticles has improved properties used in catalysis and biomedical applications. Such hybrid structures often exhibit synergistic effects, combining the properties of both materials to provide superior performance.

Iron oxide nanocubes (IONCs), known for their distinct shape, have been extensively studied for biomedical applications like magnetic hyperthermia, drug delivery, and improving MRI contrast.[4] Compared to other iron oxide nanoparticles, nanocubes offer superior magnetic properties, improving performance in hyperthermia treatments. Research indicates that IONCs have higher specific absorption rate (SAR) values than other morphologies, making them more effective for hyperthermia applications.[5] The SAR measures how much heat magnetic nanoparticles release under the applied alternating magnetic field. Factors like the size, shape, and magnetic anisotropy of the nanoparticles, as well as the strength of the magnetic field, influence the amount of heat generated.[6] Studies are ongoing to further optimize SAR values by understanding the effect of nanoparticle aggregation on heating performance. It is an active area of research as the heating efficiency can be increased or decreased depending on the nature of aggregation.[7]

In this thesis study, we focused on two main objectives: developing new green synthesis routes for AgNWs and enhancing the SAR of iron oxide nanocubes by controlling the form of aggregation. For the controlled aggregation of the system, templating and hybridization methods were followed by assembling the IONCs on AgNWs. Morphology and magnetic characterizations were carried out to investigate the effect of the structure on the magnetic behavior and SAR value.

1.2. Structure and Scope of the Thesis

The thesis's main idea and purpose are presented in the first chapter. The second and third chapters provide the background that constitutes the studies' foundations and the characterization tools, respectively. Chapter 5 explored the role of various transition metal salts in the environmentally friendly synthesis of AgNWs and highlighted their influence on the nanowires' morphology, size, and uniformity. Chapter 6 presents a new approach to achieving high performance in magnetic hyperthermia treatments. The assembly of IONCs onto AgNWs templates was shown to improve SAR and overall efficacy. The last section presents general conclusions and future prospects regarding using plasmonic and magnetic nanostructures, separately and as hybrids, in the biomedical field.

CHAPTER 2

BACKGROUND

2.1. Metal Nanostructures

Metal nanostructures stand out among inorganic nanostructures due to their extraordinary plasmonic and electronic properties. These unique properties make them suitable for new applications in biomedicine, photonics, electronics, sensing, and catalysis. Silver (Ag), gold, copper, platinum, nickel, and palladium have been the most studied metals for the latest technological advances in the last decade.[8] One crucial factor affecting metal nanostructures' usefulness is that they can be easily prepared in controllable sizes and shapes. In that sense, various nanostructures can be prepared using chemical methods with Ag, gold, and palladium.[9] Cost disparities between metals impact the applicability of metal nanostructures in technology. Ag is a more abundant and less expensive natural resource than gold and palladium. In addition, Ag has the highest thermal ($429\ W.m^{-1}K^{-1}$) and electrical ($6.30 \times 10^{7}\ S.m^{-1}$) conductivity in bulk form among the metals. One disadvantage is that Ag nanostructures, specifically Ag ions derived from nanoparticles, are considered toxic.[10] However, surface passivation can significantly increase their stability, reducing or eliminating toxicity.

2.2. Silver Nanowires

Silver nanoparticles have been extensively studied for their physical, chemical, and optical properties, which strongly rely on their size, shape, crystallinity, and surface properties. Shape control is one of the most effective tools for tailoring the properties of metal nanostructures. The size and morphology of silver nanoparticles can be tailored for the intended application. The wire, rod, triangle, right bipyramid, sphere, cube, octahedron, and rice morphologies have been studied extensively in the literature.[11,12] Silver nanowires (AgNWs) have recently received increased attention from scientists and industry. AgNWs are one-dimensional nanostructures with a high aspect ratio. For silver nanoparticles to be defined as nanowires, their aspect ratio must be greater than 10.

Generally, their diameters are approximately 10-200 nm, and their lengths are 5-100 μm.[13,14] The unique morphology of AgNWs provides distinctive properties, such as high electrical conductivity, high surface area, and surface plasmon resonance (SPR), making them handy materials for many applications.

2.3. Applications of AgNWs

AgNWs possess exceptional properties (i.e., high surface area, electrical and thermal conductivity, and SPR) that make them highly desirable for a wide range of applications in the fields of electronics, photonics, and biomedicine. They are excellent candidates for transparent conductive film fabrication due to the combination of SPR, flexibility, and conductivity. They can be used as electrode material instead of non-flexible conductive oxides in solar cells, light-emitting devices, and touch screens.[15] Due to their large surface area, conductivity, and lightweight nature, AgNWs are promising materials for electromagnetic shielding. Moreover, their unique properties make them suitable for sensing applications like electrochemical and optoelectronic sensors.[16]

Additionally, AgNWs can be used as fillers in conductive adhesives for microelectronic packaging, enhancing their electrical conductivity and mechanical properties. Another extensively researched field of AgNWs is biomedical applications.[14,17] By functionalizing their surface, they can be used in drug delivery. Furthermore, their antibacterial nature inhibits the bacteria's growth when incorporated into wound-healing dressing.

2.4. Synthesis Methods of AgNWs

Controlled synthesis of AgNWs with various aspect ratios allows for tuning their electrical, optical, thermal, and catalytic properties and improved application performance. The reported methods for AgNWs synthesis can be categorized under template and wet chemistry synthesis.[18] The template method can be divided into hard and soft templates. Wet chemistry mainly includes hydrothermal and polyol synthesis methods, which constitute the majority of the studies in the literature.

Template methods use nanoporous structures as host matrices for nanowire growth, enabling metal ions to be reduced electrochemically or chemically within the pores.[19] Carbon nanotubes, porous alumina, silica, and polycarbonate membranes are widely used as hard templates. This method allowed the preparation of AgNWs in well-defined morphology and high aspect ratio; however, the complexity of the protocols and the necessity of post-synthesis treatments (i.e., removing templates and purification) may cause the damaging of AgNWs structures. Also, this method is inconvenient for large-scale production. The researcher developed the soft template method to overcome the restrictions of hard template methods. Micelles, surfactants, and polymers can be used as soft templates, and they can be dissolved in solution after the synthesis of AgNWs.[18] Reactions are generally conducted in an aqueous medium in the presence of a reducing agent and Ag salt. Some of the reported soft templates are cetyltrimethylammonium bromide, polyvinyl alcohol, and polyethylene oxide. This method is amenable to scaling, but low yields, inhomogeneity, and aspect ratio AgNW synthesis limit its applicability.

The wet chemical synthesis method involves solvent, metal salts, reductants, oxidants, and surfactants and is carried out in the liquid phase. In this method, precise control over the morphology of the nanoparticle can be achieved by adjusting the reaction parameters, and is suitable for scale-up production. In hydrothermal synthesis, precursors prepared in an aqueous solution are generally placed in a sealed Teflon-lined autoclave and heated at high pressure and temperature in an oven to promote nucleation and growth of AgNWs.[20,21] This method makes homogeneous nanoparticle synthesis possible, but special autoclave equipment is required.

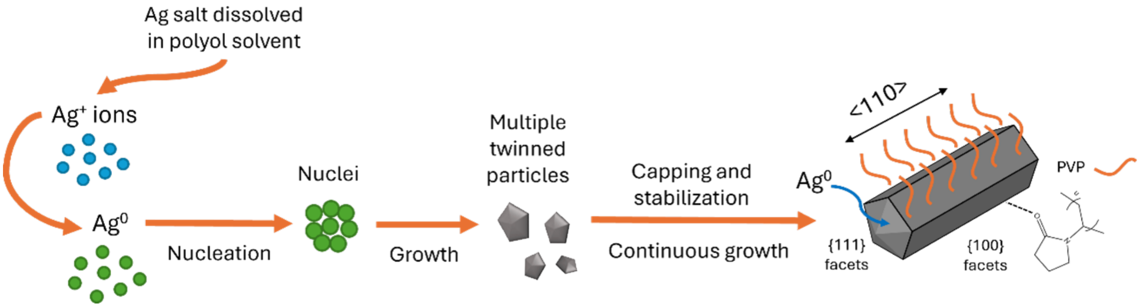

Figure 2.1. Schematic representation of silver nanowire formation in a typical polyol synthesis.

2.4.1. Polyol Synthesis of AgNWs

The polyol method is the most researched and successful method for producing AgNWs due to its simplicity, scalability, and high yield.[22] The schematic of the typical polyol synthesis of AgNWs is shown in Figure 2.1. In this method, polyols have a dual role as solvent and reducing agents. In general, polyol synthesis is carried out in the presence of polyol, silver salt, capping agent, and transition metal halide salt. Here, the polyol plays a dual role as a solvent and reducing agent in the reaction. Glycerol, ethylene glycol (EG), and propylene glycol are the most commonly used polyols in synthesizing AgNWs.[23,24] Silver nitrate ($AgNO_3$) is generally preferred as a silver source. The capping agents assist the unidirectional growth of AgNWs by capping certain facets. Also, they stabilize nanostructures and inhibit the formation of agglomeration. Polyvinylpyrrolidone (PVP) performed the best in the synthesis of AgNWs. The presence of transition metal salts (i.e., $FeCl_3$, $CuCl_2$, $CrCl_2$, $CoCl_2$, etc.) in the reaction medium ensures the scavenging of atomic oxygen from silver nanocrystallites' surfaces, electrostatic stabilization, and the formation of intermediate reaction products such as AgCl, leading to the slow release of Ag^+ ions.[25]

$$2HOCH_2CH_2OH + O_2 \rightarrow 2HOCH_2CHO\ (GA) + 2H_2O \qquad (1)$$

$$2Ag^+ + 2HOCH_2CHO \rightarrow HOCH_2COOCCH_2OH + 2Ag^0 + 2H^+ \qquad (2)$$

$$Ag^0 + (O_2) \rightarrow Ag^+ \qquad (3)$$

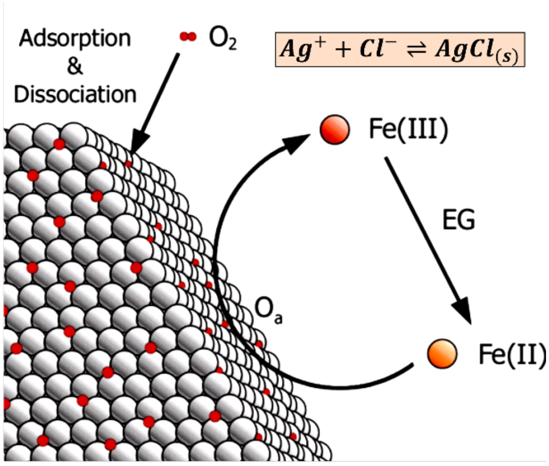

Figure 2.2. Reduction mechanism of ethylene glycol (Left) and the oxygen scavenging mechanism of the $FeCl_3$ (Right). Reproduced from reference (25).

Typical polyol synthesis begins with heating the polyol at 140-170°C for about 1-2 h before adding other precursors to increase the reducing ability of the polyol.[26] Several groups have demonstrated the effect of preheated EG on reducing activity. When EG is heated in the presence of oxygen, glycolaldehydes, a small molecule containing an aldehyde (-CH=O) and a hydroxyl group (-OH), are produced, which is a potent reducing agent for the reduction of Ag^+ to Ag^0 (Figure 2.2). To achieve a synthesis with a high aspect ratio and low by-product formation, the Ag seeds must first be gradually brought to supersaturation, which requires low reaction rates. Second, excess free oxygen must be removed from the Ag seeds' surfaces to prevent oxidative etching and growth blocking.

Transition metal halide salt is added to the reaction medium to achieve these objectives, and the mechanism will be explained via $FeCl_3$. Cl^- ions provide stabilization of Ag^+ by electrostatic interactions and bind to Ag^+ ions in solution to form AgCl, thus reducing the amount of free Ag^+ in solution and preventing initial supersaturation. The solubility of AgCl is lower than that of $AgNO_3$, so Ag^+ is released into the medium at a slow rate. In this way, the reaction rate is slowed, and anisotropic growth is promoted. When $FeCl_3$ is injected into the EG solution, Fe^{+3} is reduced to Fe^{+2}. Fe^{+2} is oxidized back to Fe^{+3} by scavenging oxygen from the Ag seed surface and can be reduced by EG again. The process continues as iron continuously fluctuates between +2 and +3 oxidation states. In that way, the dissolution of silver from the formed nanocrystals can be prevented.

Finally, PVP is added to the reaction medium before or simultaneously with the addition of $AgNO_3$.[27–29] Sun et al. reported that multiple twinned particles (MTP) and PVP are required for growth in nanowire morphology.[26] MTP has 5-fold symmetry, and ten {111} facets connect its surfaces. They indicated that polyol synthesis favors the formation of decahedral MTPs to minimize the surface energy. Each {111} facet forms a {100} facet perpendicular to the nanowire's longest dimension (Figure 2.1). The twin boundaries are the highest energy regions on the MTP surface and thus help the diffusion of silver atoms from the solution to these areas. PVP polymers form a complex with Ag^+ via the N-C=O group on their chain. Studies have shown that the affinity of PVP for {100} facets is much stronger than for {111} facets. Thus, stabilizing with PVP can reduce the growth rate of newly formed {100} facets, and AgNWs grown in a specific direction are obtained.

2.4.2. Effective Parameters on Polyol Synthesis

The fine-tuning of several parameters allows the size adjustment of the AgNWs: temperature, stirring rate, the molecular weight of the PVP, the molar ratio of precursors, and the type of transition metal salt.[30–33] Temperature is the main factor for converting EG to glycolaldehydes and reducing Ag^+ to Ag^0. A high temperature (110-200 °C) is required for these reactions. Also, low temperatures are insufficient for the formation of MTP. Studies showed that high aspect ratio AgNWs can be achieved between 140-180 °C. Bergin et al. reported that longer AgNWs (20 μm and 65 nm) were obtained at 130 °C, whereas shorter but thinner AgNWs (7.5 μm and 45 nm) were obtained at 160 °C.[34] AgNWs with desired properties can be obtained by maintaining a uniform mass and heat transfer rate during polyol synthesis. Researchers reported that the stirring rate influences the final length and diameter of the AgNWs. It has been shown that the high stirring rate (700-800 rpm) results in shorter AgNWs but with the formation of various other nanoparticle morphology.[30,35] This may be explained by the increased oxidative etching of particles with increasing mixing speed. A lower stirring rate (100-300 rpm) allows the synthesis of longer AgNWs, while the diameter of the nanowire decreases with increasing stirring rate. The adsorption of PVP on the silver surface and the steric effect it creates vary with molecular weight and thus influence the morphology of AgNWs. Several studies showed that high molecular weight PVP tends to result in higher length and smaller diameter AgNWs morphology.[36] Another parameter that strongly affects the final morphology of AgNWs is the molar ratio of PVP to $AgNO_3$ (PVP: $AgNO_3$). It has been reported that particles with different morphologies are formed at high molar ratios due to the coverage of other facets than {100} facets. At lower molar ratios, the amount of PVP is insufficient to passivate the {100} facets; thus, shorter and larger diameter AgNWs are obtained. Coskun et al. reported the optimum value as 7.5:1 in their experimental conditions.[30] The length and diameter of AgNWs are affected by transition metal salt, but few studies have been conducted to investigate this effect.

2.5. Magnetism

Magnetism results from electron spin and orbital motion interaction in atoms, leading to atomic magnetic moments.[37] The interactions between atomic magnetic moments are called exchange interactions. Among the different forms of magnetism, diamagnets and paramagnets exhibit no exchange interaction, while ferromagnets, antiferromagnets, and ferrimagnets show strong interactions. The response of a material as a function of externally applied magnetic fields and temperature determines its form of magnetism.[38]

Magnetic materials can be classified as non-magnetic and magnetic. The diamagnets, paramagnets, and antiferromagnets are classified as non-magnetic due to their lack of net magnetic moment under the zero field. The vector sum of the orbital and spin magnetic moments gives the net magnetic moment. The magnetic moments of diamagnetic materials are induced under a non-zero magnetic field and are aligned in the opposite direction to the applied field. This response originates from the change in the orbital motion of electrons and does not show a strong temperature dependence. Unlike the diamagnets, the magnetic moments of paramagnets aligned in the same direction with the applied magnetic field due to their unpaired electrons, which exhibit strong temperature dependence. Antiferromagnets have shown strong exchange interactions below a critical Néel temperature. In the zero field, an antiferromagnet's net magnetic moment is zero because the moments of neighboring atoms or ions align antiparallel to their neighbors. Above the Néel temperature, the material behaves as a paramagnet.

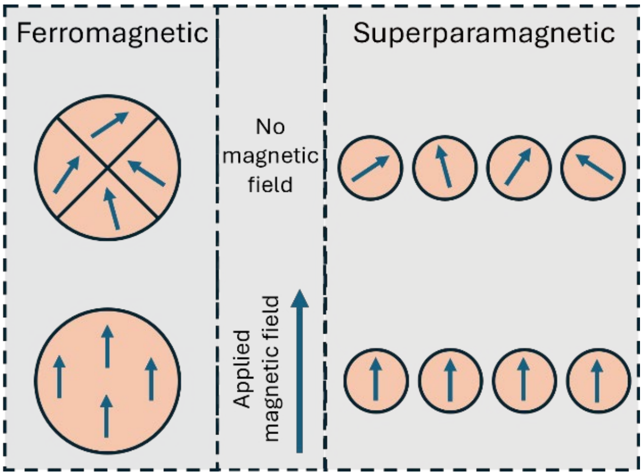

Figure 2.3. Magnetic moments in ferromagnetic and superparamagnetic materials.

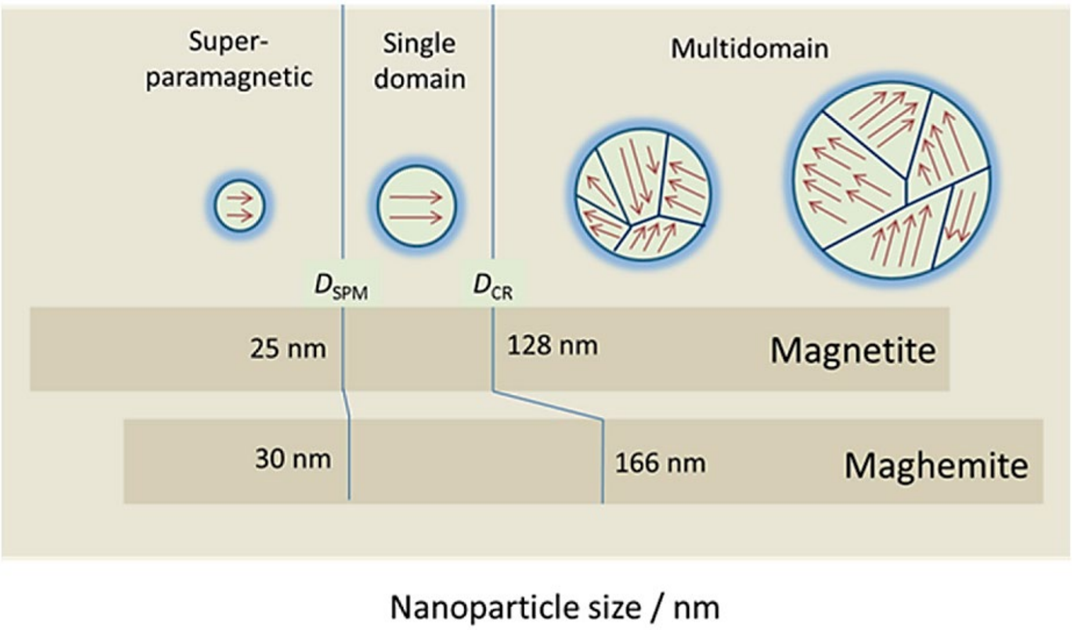

Figure 2.4. Size-dependent superparamagnetic, single-domain, and multi-domain magnetic regimes of magnetite and maghemite. Reproduced with permission.[39] Copyright © 2015 Estelrichet al. MDPI.

On the other hand, ferromagnets and ferrimagnets are classified as magnetic materials due to having a net magnetic moment in the absence of a magnetic field. Ferromagnetic materials have strong exchange interactions, and below the Curie temperature, the atomic magnetic moments are aligned parallel to their neighbors. Above the Curie temperature, the material behaves as a paramagnet. Ferrimagnets also show strong exchange interaction, but unlike ferromagnetism, where all magnetic moments are aligned parallel, ferrimagnetism results in a net magnetic moment due to the unequal magnitudes of the parallel and antiparallel magnetic moments. The magnetic phases of iron oxides, which are magnetite (Fe_3O_4) and maghemite (γ-Fe_2O_3), are actually ferrimagnetic. Magnetite has a spinel crystal structure (AB_2O_4). The formation of net magnetic moment in magnetite lies under the following steps: (i) the Fe^{2+} and Fe^{3+} ions occupy different lattice sites, leading to a specific arrangement of magnetic moments. Net magnetic moments of Fe^{2+} and Fe^{3+} ions are 4 and 5 Bohr magnetons, respectively. (ii) The magnetic moments of the Fe^{2+} and Fe^{3+} ions are aligned in opposite directions. (iii) Due to the unequal magnitudes of the magnetic moments, the antiparallel alignment does not entirely cancel out. This results in a net magnetic moment.

2.6. Superparamagnetic Iron Oxide Nanoparticles

The bulk forms of ferromagnetic materials consist of many small magnetic dipole regions called domains. Domains are separated by domain walls, transition regions of finite thickness where the direction of magnetization changes gradually from one side to the other.[40] All magnetic dipoles are aligned in the same direction inside the domains by exchanging forces (Figure 2.3).[38] The multidomain structure of bulk ferromagnets is based on the reduction of magnetostatic energy. Magnetostatic energy is associated with the magnetic field created by the magnetization within a material. As the volume of a material increases, the number of magnetic domains tends to increase to minimize the magnetostatic energy. This is because having multiple domains with opposing magnetization can reduce the overall magnetic field outside the material. If the size of a ferromagnetic material is reduced below the critical diameter, D_{cr}, the domain walls are eliminated, and the material becomes a single domain. In essence, forming domain walls is a trade-off between minimizing magnetostatic energy and the energy cost of creating domain walls. When the material is small enough, the energy cost of domain walls outweighs the benefits of reducing magnetostatic energy, leading to a single-domain state.[39]

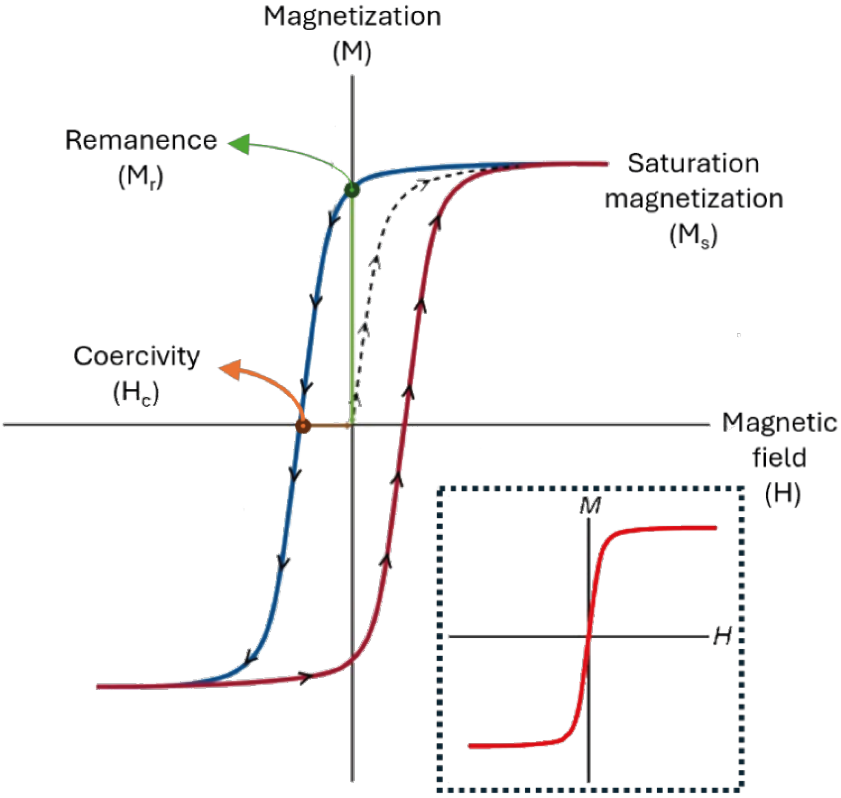

Figure 2.5. The M-H curve for a ferromagnetic material. The lower right inset shows the M-H curve for a superparamagnetic material. Reproduced with permission.[39] Copyright © 2015 Estelrichet al. MDPI.

The size-dependent magnetic regimes of magnetite and maghemite are given in Figure 2.4. The D_{cr} value varies depending on the material and is generally a few tens of nanometers. If the size of a single-domain particle is further reduced below the superparamagnetic diameter, D_{spm}, the thermal energy (kT) becomes equal to or greater than the energy barrier between the easy axes, causing the magnetization direction to fluctuate randomly—this kind of system named as superparamagnet. The magnetization of the system fluctuates randomly due to thermal energy, and there is no permanent magnetization in the absence of an applied field. Under external magnetic fields, superparamagnetic materials behave similarly to paramagnetics. However, rather than every atom being affected differently by the magnetic field, the crystallite's magnetic moment aligns with the field for the superparamagnetic materials.

The relationship between an applied magnetic field and the resulting magnetization in a ferromagnetic nanoparticle is well described by a hysteresis loop (Figure 2.5).[39] The data of coercive field (H_c), saturation magnetization (M_s), remanence (M_r), and susceptibility (χ) can be determined from the magnetization curve. H_c is defined as the maximum external magnetic field strength required to reduce the magnetization of a material to zero after it has been fully magnetized. M_s is the point at which all the magnetic moments within the material are aligned in the same direction. It is the highest magnetization that the material can reach. M_r is the magnetization preserved in a material after removing the external magnetic field. The following equation, $M=\chi H$, determines susceptibility. It measures a material's response to an applied magnetic field and quantifies how easily it can be magnetized.

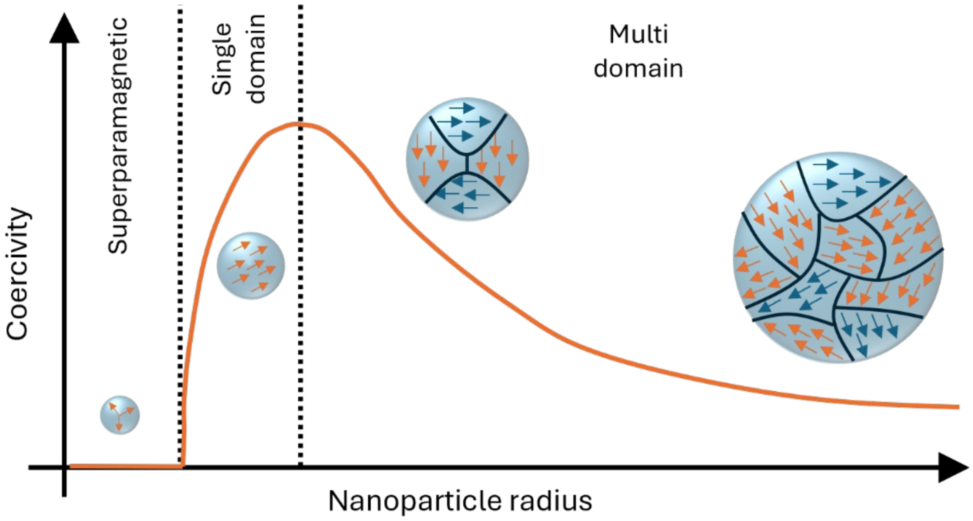

Figure 2.6. Schematic illustration of the coercivity-size relations.[38]

Typically, in static magnetization, where the direct current (DC) magnetic field is applied and changes slowly, superparamagnetic nanoparticles do not exhibit significant M_r and H_c. They lack hysteresis and follow the same sigmoidal curve because the magnetic moments have enough time to adjust to the changing field, and the system remains in equilibrium (Figure 2.5 inset). Also, the dependence of coercivity on size is shown in Figure 2.6. The coercivity increases to a maximum with decreasing particle size; as the particle size decreases below the critical diameter, the material becomes superparamagnetic, and the coercivity drops to zero.[38]

Superparamagnetic iron oxide nanoparticles (SPIONs) can exhibit a wider hysteresis loop in dynamic magnetization, where the alternating current (AC) magnetic field is applied, and frequency changes rapidly. The reason is the relative difference between the measurement time (τ_m) and the nanoparticle's effective relaxation time (τ). The magnetic moments do not have enough time to fully relax and align with the changing field, leading to a delayed response and energy loss. In summary, if $\tau_m > \tau$, the nanoparticles are in the superparamagnetic regime, and if $\tau_m < \tau$, the nanoparticles are in the blocked regime, also called the ferromagnetic regime.[41]

2.7. Magnetic Hyperthermia Therapy Applications of SPIONs

SPIONs have emerged as a versatile platform for various applications such as biomedical, environmental, magnetic fluids, and catalysis.[42] Their unique properties, including their high surface-to-volume ratio, biocompatibility, and magnetic properties, make them promising materials for these applications. Biomedical applications of SPIONs are mainly focused on cancer therapy, with prominent applications being drug delivery, magnetic resonance imaging contrast agents, and magnetic hyperthermia therapy (MHT).[39,42] SPIONs are widely studied in drug delivery applications due to their stability, surface accessibility for functionalization, and high drug-loading capacity. With an external magnetic field, surface-functionalized and drug-loaded particles can act locally by releasing the drug, thus reducing side effects and the dosage required. In magnetic resonance imaging, SPIONs are used as contrast agents to enhance image contrast and improve the visualization of specific tissues and organs. SPIONs accumulated in targeted tissues have a strong magnetic moment that can significantly alter the surrounding magnetic field; the MRI scanner can detect these changes in the magnetic field and result in increased signal intensity.[43,44] Magnetic hyperthermia application and the requirement of particles for effective heat generation will be discussed in detail below because the nanoparticles synthesized in this thesis were being investigated for potential hyperthermia uses.

2.8. Effective Parameters on Specific Absorption Rate

MHT is one of the most promising applications of SPIONs. MHT is a non-invasive cancer treatment that uses magnetic nanoparticles and alternating magnetic fields to generate heat. The heat generated by magnetic nanoparticles is used to raise the temperature of targeted tumor tissue to a level (42-46°C) that can destroy cancer cells without harming healthy tissue.[37,38] The heating efficiency of the SPIONs can be defined as a specific absorption rate (SAR) or specific loss power (SLP). SAR measures how much electromagnetic energy is absorbed by magnetic nanoparticles (MNP) per unit mass and converted to heat under an applied magnetic field. SAR can be described as the equation below, where "P" is the dissipated heat power, "ρ" is the density of MNP, "A" is the area of the hysteresis loop, and the "f" is the frequency of the applied magnetic field. Its unit is watts per gram (W/g).

$$SAR = \frac{P}{\rho} = \frac{A \times f}{\rho} \tag{1}$$

Synthesis and design of nanoparticles with high heating power allows for greater SAR values. A high SAR value is vital for reducing MNP-related side effects by reducing the dose required in the tumor area.[45] The heat generation of the magnetic nanoparticle is related to its hysteresis loop area. The area of the hysteresis loop represents the energy lost per cycle of magnetization reversal. A broader cycle requires more energy to magnetize and demagnetize the material, dissipating excess energy as heat. It has been shown that the SAR values of SPIONs generally increase with applied magnetic field strength (H_{AC}, A.m^{-1}) and frequency (s^{-1}). However, the $H_{AC}.f$ factor is kept below the $5 \times 10^9\ A.m^{-1}.s^{-1}$ value that is clinically suitable to avoid the formation of eddy currents in tissue.

The SAR value is also affected by the shape and size of the hysteresis loop features of SPIONs, which is influenced by several factors, such as particle size, shape, chemical composition and crystalline phase, surface modifications, and controlled assembly.[38,41,45,46] Also, external factors such as temperature and surrounding medium affect the magnetization curves. The magnetization of SPIONs generally decreases as their particle size decreases due to the surface-to-volume ratio. The surface interactions and defects are pronounced and may inhibit the alignment of magnetic moments perfectly parallel to the magnetic field. Such misalignment may cause the spin canting and spin-spin exchange coupling, reducing magnetization.[38,45] The shape of the nanoparticles can affect their magnetic anisotropy. For instance, it has been shown that cubic SPIONs have higher SAR values due to low surface spin disorder by owing flat cube surfaces compared to spherical counterparts. The nanoparticles' chemical composition and crystal structure have a crucial effect on magnetization. The doping of the SPIONs with divalent metal ions and the arrangement of iron ions in the crystalline lattice determines the magnetic properties.[47] Self-assembled nanostructures such as clusters, chains, and columns can be regulated by surface modification of SPIONs[5,7,38,46,48–50] (Figure 2.7).

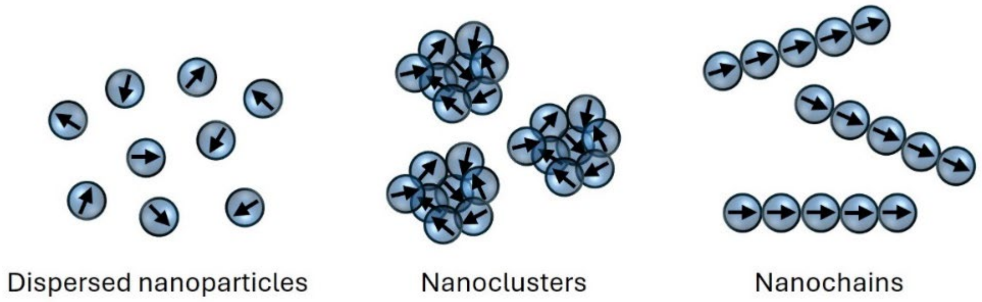

Figure 2.7. Schematic representation of various nanoassemblies that can form under an applied AC magnetic field.

Such structures can reduce or increase the area of the magnetization curve due to the interaction between the magnetic dipoles of the neighboring nanoparticles. Several studies showed that the random aggregation of nanoparticles into clusters can hinder the alignment of magnetic moments and lead to antiferromagnetic coupling, suppressing the overall magnetization and reducing heat generation efficiency. Also, the formation of random clusters can reduce their mobility and magnetic moments, creating a magnetic flux closure configuration that reduces their interaction with other clusters.[45,51] However, in the case of chain formation, magnetic nanoparticle alignments promote dipolar coupling between the particles, thus increasing effective anisotropy. The enhanced anisotropy makes the magnetic moments more resistant to reorientation under alternating magnetic fields, resulting in increased hysteresis losses and higher SAR values.

2.9. Synthesis Methods of SPIONs for MHT

The performance of MNPs in MHT applications largely depends on the diameter, shape, crystallinity, and particle size distribution of the synthesized nanocrystal. Studies showed that the MNP with high crystallinity, crystalline anisotropy, and monodisperse particle size distribution provides higher SAR values. Therefore, the synthesis method of magnetic nanoparticles is critical.[52] SPIONs can be prepared using a variety of physical or chemical methods. Among the bottom-up chemical synthesis methods, co-precipitation, thermal decomposition, and solvothermal have been widely studied in the literature.[53]

Co-precipitation is a standard synthesis method, also called Massart's method, which involves the precipitation of ferrous (Fe^{+2}) and ferric (Fe^{+3}) salt (i.e., chlorides, sulfates, and nitrates) solutions in an alkaline medium.[54] The size and the shape of the MNP can be varied by adjusting the type of salts, ionic strength and pH of medium, temperature, and time. The hydroxyl groups on the surfaces of the synthesized particles make them water-dispersible, excluding the need for additional surface modification steps. This method is simple and inexpensive and allows the production of large quantities of nanoparticles in a single batch. However, the resulting nanoparticles generally have low crystallinity due to the rapid increase in particle size during the process. In addition, the synthesized nanoparticles tend to have a broad size distribution and aggregation.

In the thermal decomposition method, organometallic precursor (i.e., iron pentacarbonyl, acetylacetonate, and oleate) is decomposed at high temperatures (generally above 200°C) in apolar organic solvents with the inclusion of surfactants.[55] The presence of surfactants allows the synthesis of geometrically well-defined nanocrystals by passivating the growth along some crystal facets. Some of the most used surfactants are oleic acid, decanoic acid, oleylamine, and hexadecylamine. Nanocrystal surfaces synthesized by this method are hydrophobic and require a post-synthetic ligand exchange strategy for biological applications. With this method, nanocrystals with high crystallinity and monodisperse particle size distribution can be produced while providing good control over the size and shape of the nanocrystal. However, thermal decomposition requires high reaction temperatures and a complex process with multiple steps, allowing milligram-scale particle synthesis. When scaling is attempted, a loss of control over particle size, size distribution, and shape has been observed.

Solvothermal synthesis is an effective and versatile method for creating iron oxide nanoparticles with specific properties.[56] In this method, typically, a solution is prepared by dissolving iron precursors (i.e., organometallic iron complexes or iron salts) in alcohol, and the prepared precursor solution is transferred to a sealed autoclave reactor. The reactor is generally placed in an oven at high temperature, providing high pressure to promote the nucleation and growth of high-crystallinity nanocrystals. The alcohols are very useful solvents in the solvothermal method due to their ability to dissolve polar and non-polar compounds in a wide range and the vapor pressure they provide. The nanocrystals' shape and dimensions can be controlled by the parameters of the solvent polarity, precursor concentrations, type of iron source and shape-directing agents, sealed autoclave reactor filling ratio, temperature, and time. The surfaces of the synthesized nanoparticles can be hydrophilic or hydrophobic, depending on the selected surfactant. By carefully controlling the influencing parameters, highly crystalline nanocrystals with the desired size and shape can be produced via solvothermal synthesis. Furthermore, this method can be scaled up to produce large quantities of nanoparticles by allowing multiple parallel syntheses in the oven.

CHAPTER 3

ANALYTICAL TOOLS FOR MATERIAL CHARACTERIZATION

3.1. Optical Characterization

Ultraviolet-Visible (UV-Vis) spectroscopy is an empirical method for measuring the amount of light absorbed or transmitted by a sample at the electromagnetic spectrum's ultraviolet and visible light wavelengths. The UV generally ranges from 100 to 400 nm, while the Vis range is approximately 400 to 800 nm. It is a widely used technique to characterize the unique optical properties of metal nanoparticles. When exposed to light, metal nanoparticles exhibit a distinct absorption peak called the localized surface plasmon resonance (LSPR) band.[57] This peak is very sensitive to changes in the nanoparticle's size, shape, and composition, as well as the dielectric properties of the surrounding medium.

Metal nanoparticles have free electrons on their surfaces that are not tightly bound to atoms. Free electrons oscillate collectively at a specific frequency when they interact with light. At that resonant frequency, the oscillation of the electrons is in phase with the incident light. The interaction can result in the absorption or scattering of light. This phenomenon is named LSPR, and the schematic of the principle is shown in Figure 3.1.

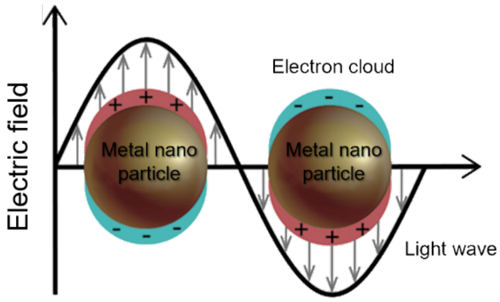

Figure 3.1. Schematic of LSPR principle. Reproduced from reference (57).

Haman et al. investigated the connection between the optical properties of silver nanowires and their shape by using a finite difference time domain simulation method. They showed that accurate structural information can be extracted from UV–vis spectroscopy. The excitation of transverse plasmon resonances causes the characteristic

UV extinction peaks of AgNWs, as shown in Figure 3.2.[58] Specifically, a double extinction peak in the spectrum suggests that the nanowires have a pentagonal cross-section.

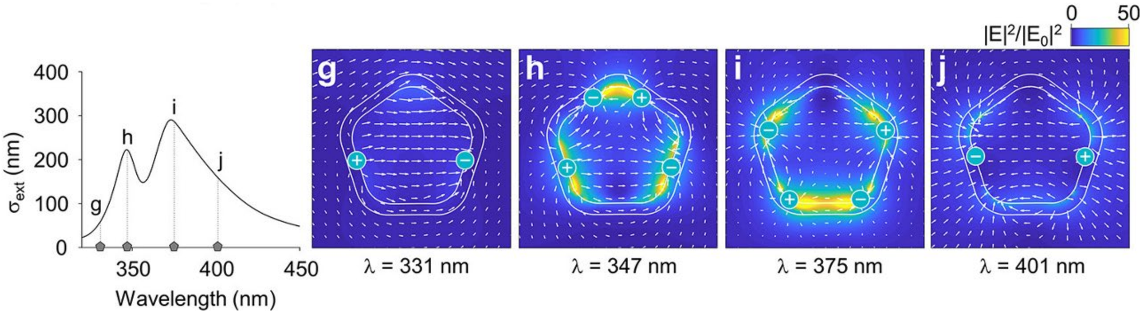

Figure 3.2. The simulated extinction cross-section for an infinite pentagonal AgNW. Reproduced with permission.[58] Copyright © 2022 Hamans et al. Published by American Chemical Society

Extinction measurements of the AgNWs were carried out using an Agilent Cary 300 UV-Vis spectrophotometer and Ocean Optics setup (which involves a balanced deuterium–tungsten halogen light source, DH2000-BAL, Ocean Optics, and a fiber-coupled spectrometer, USB4000, Ocean Optics).

3.2. Size and Zeta Potential Analysis

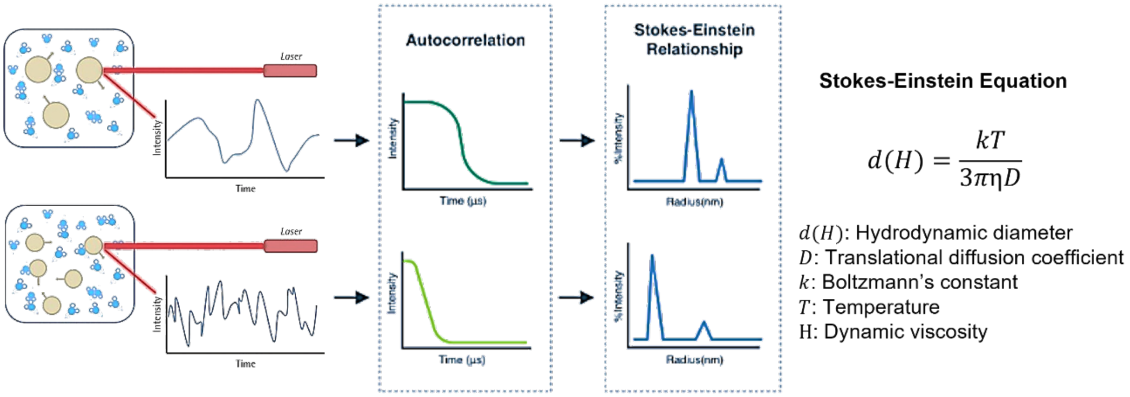

Figure 3.3. Working principle of DLS for the determination of the hydrodynamic radius of IONCs. Reproduced from reference.[59] Copyright © 2014 The Korean Society of Environmental Health and Toxicology

Dynamic light scattering (DLS) is an analytical technique based on the Brownian motion principle, which states that particles suspended in a liquid move randomly as they collide with solvent molecules. These collisions cause a certain amount of energy to be transferred to the particle, thus activating the particle's motion. The amount of energy transferred is considered constant for all particles, so it has a greater effect on small particles, causing small particles to undergo faster Brownian motion than large particles.

The hydrodynamic radius of the sample can be analyzed using DLS (Figure 3.3).[59] In the DLS setup, a laser is directed onto a cuvette containing a colloidal nanoparticle solution. The particle movements cause light to scatter in different directions, and the intensity of the scattered light varies over time. These changes in the light intensity are analyzed using a correlator to determine the diffusion coefficient of the particles. The diffusion coefficient is directly related to the hydrodynamic radius of the particles, and when other parameters are known, the hydrodynamic radius can be calculated. The hydrodynamic radius of iron oxide nanocubes (IONCs) with various surface modifications was analyzed using the Zetasizer Nano ZS90 instrument (Malvern Panalytical, United Kingdom) in water and with a disposable cuvette.

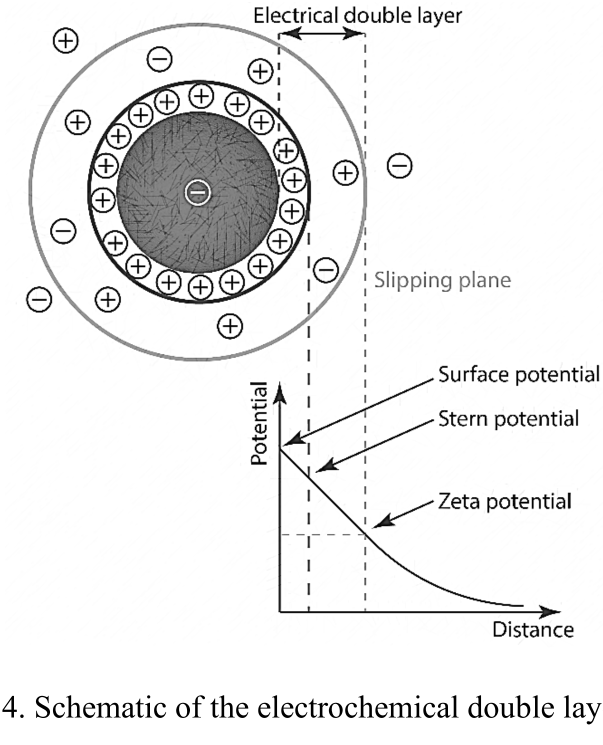

Figure 3.4. Schematic of the electrochemical double layer.

Zeta potential, or electrokinetic potential, is a measurement of a nanoparticle's surface charge in a liquid, usually expressed in millivolts (mV) (Figure 3.4). It is an essential parameter for determining the stability and behavior of colloidal dispersions. Knowing the zeta potential of nanoparticles is also important for understanding their interactions with other materials. The zeta potential's magnitude indicates the colloid's stability, and its sign indicates whether the surface is positively or negatively charged. Absolute zeta potential values greater than ±30 mV indicate stable dispersion due to electrostatic repulsion, preventing particles from coming into close contact. Aggregation or flocculation is more likely at zeta potentials below ±30 mV.

In this thesis, zeta potential measurements were performed using the Zetasizer Nano ZS90 instrument (Malvern Panalytical, United Kingdom). This device uses a combination of laser Doppler velocimetry and phase-analyzed light scattering (PALS) to measure particle electrophoretic mobility. Electrophoretic mobility indicates the speed at which a charged particle moves in an electric field. For this measurement, the nanoparticle colloid is transferred into a measuring cuvette equipped with an electrode with a known distance, and a potential is applied to the electrodes. Under the applied field, particles move toward the electrodes with the opposite charge. The laser beam is directed to the sample, and the Doppler shift of the scattered light is used to determine the velocity of the particles. The zeta potential is then calculated from the electrophoretic mobility using the Helmholtz-Smoluchowski equation.

3.3. Morphological Characterization

Scanning electron microscopy (SEM) is an imaging technique that enables the observation and characterization of organic and inorganic materials at the nanometer scale. SEM uses a focused electron beam to raster across a sample. The signals emitted from the beam specimen interaction are collected by the detectors and processed to extract information about the sample topography, composition, and microstructure. In this study, JEOL JSM-6490LA and FEI Quanta 250 FEG SEM instruments were used. The secondary electron detector of SEM was used to determine the size and morphology of the synthesized nanoparticles.

Transmission electron microscopy (TEM) was used where the resolution of SEM was insufficient in determining the size and morphology of the nanoparticles. In TEM, a thin sample (typically less than 100 nm thick) is placed in the path of a focused electron beam. As the electrons interact with the sample, some are transmitted through while others are scattered. An objective lens then focuses the transmitted electrons onto a fluorescent screen or a charge-coupled device (CCD) camera. The resulting image shows variations in electron intensity, with darker areas representing regions of the sample that have transmitted fewer electrons and lighter areas representing regions with higher electron transmission. A JEOL JEM-1400 microscope with an accelerating voltage of 120 kV was used to obtain bright-field TEM images of the IONCs and IONCs-AgNWs for the size, morphology, and assembled structure analysis. TEM samples were prepared by dropping diluted nanoparticle solutions onto 200 mesh carbon-coated copper grids.

3.4. Structural Characterization

X-ray diffraction (XRD) is a technique for determining materials' crystallographic structure, phase composition, and structural properties. It is useful for characterizing nanomaterials and gaining insight into their crystalline structure. XRD is based on the principle of constructive interference of X-rays scattered by atoms in a crystal lattice. When X-rays are focused on a crystalline sample, they diffract at specific angles (Bragg's Law). The resulting diffraction pattern is measured and analyzed to determine the material's structure.

The XRD technique was used to demonstrate that the crystalline phase of IONCs exposed to various chemical reactions during surface functionalization remained intact. The XRD pattern of the nanoparticles was realized using a PANalytical Empyrean X-ray diffractometer equipped with a 1.8 kW Cu Kα ceramic X-ray tube and a PIXcel3D 2×2 area detector operating at 45 kV and 40 mA. Samples were prepared by dropping concentrated nanoparticle solutions onto a zero-diffraction quartz wafer.

3.5. Chemical Characterization

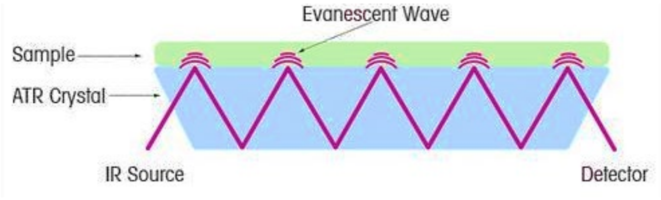

Figure 3.5. The principle of ATR-FTIR spectroscopy.

The surface chemistry of the IONCs with various surface modifications was analyzed by Fourier transform infrared spectroscopy with an attenuated total reflectance configuration (ATR-FTIR) using a Vertex 70V Bruker instrument. ATR-FTIR is an effective method for studying functional groups and molecular structures on the surface of nanoparticles. ATR-FTIR works based on infrared absorption spectroscopy. The infrared beam is directed into a high refractive index crystal, which is reflected multiple times internally (Figure 3.5). When the beam reaches the sample and contacts the ATR crystal, some infrared light penetrates the sample's surface, causing molecular vibrations that absorb certain wavelengths. The resulting spectrum represents the vibrational modes that provide information about the sample's chemical composition.

Inductively coupled plasma-optical emission spectrometry (ICP-OES) was used to determine the iron concentration in the solution required for the AC magnetometer measurements. ICP-OES is an analytical technique used for elemental analysis of materials. It uses inductively coupled plasma to excite atoms in a sample. A sample, usually liquid, is aerosolized and introduced into a plasma torch, exposed to high temperatures of about 10,000 K. The intense energy exposure excites the electrons of the atoms, causing them to emit light at characteristic wavelengths as they return to their ground state. The emitted light is then analyzed with a spectrometer to identify and quantify the elements in the sample.

ThermoFisher iCAP 6000 series ICP-OES spectrometer was used for elemental analysis. To carry out ICP-OES analysis, 10 μL of nanoparticle solution was added to 1 mL of aqua regia and left overnight for digestion. The sample solution was then diluted to 10 mL by adding Milli-Q water and filtered through a 0.45 μm PTFE membrane.

3.6. Magnetic Characterization

The magnetic properties of IONCs samples (coercivity, remanence, saturation magnetization, field, and SAR values) were determined using an AC magnetometer with three runs per measurement. The AC Hyster Advance (Nanotech solutions) instrument was used for the measurements. It is an automated inductive magnetometer that can determine the sample's SAR value with more than 95% accuracy under a controlled temperature environment.

To conduct the AC magnetometer analysis, 40 μL of sample solution with a known iron dose ($g.L^{-1}$) was placed in a glass tube. Measurements were performed under the specific magnetic field frequencies (i.e., 110, 200, and 300 kHz) and strengths (i.e., 12, 16, and 24 $kA.m^{-1}$). The SAR value is determined from the equation below, where "A" is the area of the hysteresis loop, "f" is the frequency of the applied magnetic field, and "m" is the iron concentration.

$$SAR = A \times \frac{f}{m} \qquad (2)$$

CHAPTER 4

EFFECT OF TRANSITION METAL SALTS ON THE GREEN SYNTHESIS OF SILVER NANOWIRES

4.1. Introduction

Silver nanowires (AgNWs) are promising materials for various applications due to their exceptional optoelectronic, electrical, and thermal properties.[60] Their superior conductivity, surpassing that of other metals, makes them valuable in diverse fields. AgNWs have been synthesized using various methods, such as electroplating on a template, surfactant templating, hydrothermal and solvothermal, and polyol synthesis.[61–63] Among the synthetic methods, the polyol method is straightforward and cost-effective in synthesizing AgNWs with high yield, high aspect ratio, and uniform-sized product formation.[64] In a typical polyol synthesis of AgNWs, (i) ethylene glycol is used as both a solvent and a reducing agent at high temperatures, (ii) $AgNO_3$ as a silver precursor, and (iii) PVP as a stabilizer. It has been shown that PVP leads to one-dimensional growth of the nanoparticles due to its higher affinity to the {100} facets (i.e., side surfaces) of the silver nanoparticles than to the {111} facets (i.e., end surfaces).[65]

Ethylene glycol has been widely used in the polyol synthesis of AgNWs, but it is more advantageous to use glycerol instead. However, the polyol synthesis of AgNWs in glycerol has not been studied extensively, and transition metal salts have not been used as promoters in the polyol synthesis of AgNWs in glycerol. Here, we investigate transition metal salts that enable the synthesis of AgNWs polyol in glycerol, which acts as a solvent and reducing agent. The use of glycerol is more advantageous in the synthesis of AgNWs due to the following reasons: (i) compared with ethylene glycol, glycerol is a non-toxic, non-volatile, edible, biodegradable, and recyclable substance; (ii) glycerol has three hydroxyl functional groups, which provide stronger reducing power than ethylene glycol; and (iii) due to the high boiling point of glycerol (290 °C) (the boiling point of ethylene glycol is about 200 °C), it is possible to carry out reactions at high temperatures safely.[66] To the best of our knowledge, there has not been any report on the transition metal salts enabling polyol synthesis of silver nanowires in glycerol. Furthermore, in this study, water was used as a second solvent to facilitate the preparation of $AgNO_3$ and PVP solutions since it is impossible to completely dissolve $AgNO_3$ and PVP in glycerol without water.

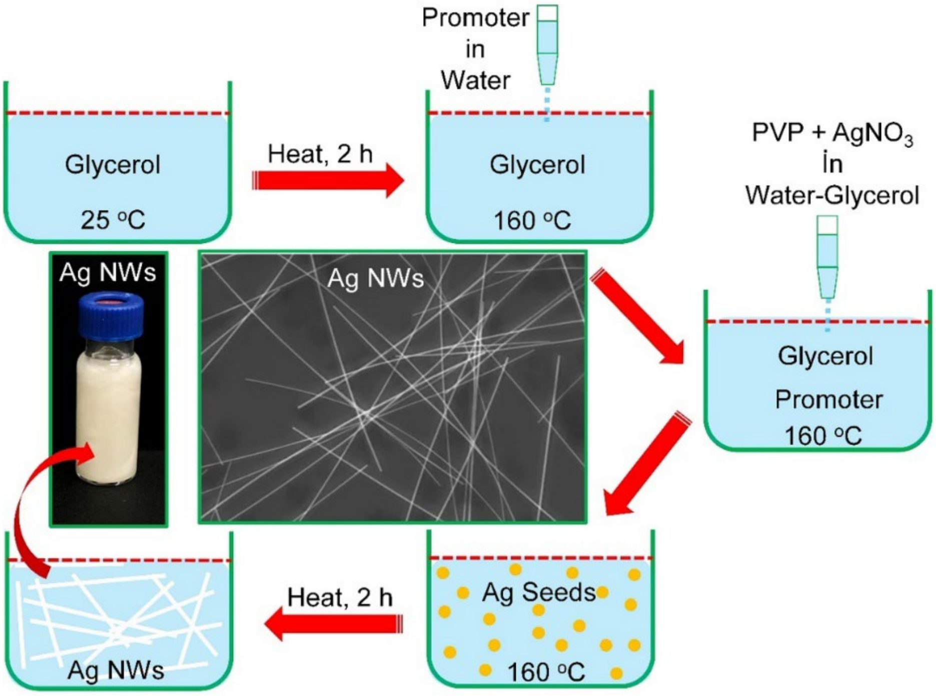

Figure 4.1. Schematic representation of the green synthesis of AgNWs.

4.2. Materials and Methods

Silver nitrate ($AgNO_3$) was purchased from Merck. Glycerol anhydrous (≥*99.5*%) and polyvinylpyrrolidone (PVP, average M_w ~1,300,000 and M_w ~40,000) were all purchased from Sigma Aldrich and used without any further purification. Milli-Q water with a resistivity of 18.2 MΩ.cm at 25 °C was used in all the experiments.

AgNWs were dispersed in isopropyl alcohol and drop cast on silicon substrate for morphology characterization by SEM (SEM; Quanta 250, FEI, Hillsboro, OR, USA). The length and diameter measurements of the AgNWs were determined on the SEM images using ImageJ software based on at least 100 measurements. Extinction measurements of the AgNWs were conducted in a 1 cm quartz cuvette using a balanced deuterium–tungsten halogen light source (DH2000-BAL, Ocean Optics) and a fiber-coupled spectrometer (USB4000, Ocean Optics) as a UV-Vis spectrophotometry.

The AgNWs were synthesized using the salt-mediated polyol method. The method contains a polyol solvent, a silver source, a stabilizing agent, and a transition metal salt as a promoter. Glycerol was used as both a solvent and a reducing agent. $AgNO_3$ and PVP

(Mw ~1,300,000) were used as a silver precursor and a stabilizing agent, respectively. As transition metal salt, copper(II) chloride dihydrate ($CuCl_2.2H_2O$), manganese(II) chloride tetrahydrate ($MnCl_2.4H_2O$), iron(III) chloride hexahydrate ($FeCl_3.6H_2O$), cobalt(II) chloride hexahydrate ($CoCl_2.6H_2O$), chromium(III) chloride hexahydrate ($CrCl_3.6H_2O$), and zinc chloride ($ZnCl_2$) were separately used. In a typical synthesis, 5 mL of Glycerol was first transferred into a reaction vial and heated to 160 °C. Glycerol was heated in an oil bath for about 2 h under magnetic stirring at 200 rpm. Subsequently, 0.16 mL of 4 mM transition metal salt solution promoter was prepared in water and added to the hot Glycerol in a single shot. After 10 min of addition of the promoter, 2.5 mL of 0.1 M $AgNO_3$ (in 0.5 mL of water and 2.0 mL of Glycerol) and 2.5 mL of 0.6 M PVP (in 1.5 mL of water and 0.5 mL of Glycerol) were mixed and then added into the reaction mixture drop by drop. Finally, the reaction mixture was heated at 160 °C for another 2 h to complete the synthesis of AgNWs. Unless otherwise stated, the reaction was stirred at 200 rpm throughout the synthesis. When the reaction was completed, the mixture was removed from the oil bath and cooled in an ice bath. To track the AgNWs formation, 0.2 mL of the aliquot was taken and dispersed in isopropyl alcohol every 10 min. after adding the silver precursor.

For the purification step, the anti-solvent method was used. After the reaction was completed and cooled to room temperature, 20.0 mL of water was added. Then, the precise amount of the sample was taken to a separate vial, and acetone was added slowly and dropwise into the diluted solution to separate long AgNWs from the Ag nanoparticles. When precipitation was observed in the solution, the acetone addition was stopped, and the solution was left for approximately 10 min. to complete precipitation. The supernatant was carefully removed by using a pipette. Afterward, the precipitate was redispersed in PVP solution in water (0.5 % w/w, Mw ~40,000). This procedure was repeated four times to complete the purification of AgNWs. Subsequently, the precipitate of AgNWs was redispersed in isopropyl alcohol and centrifuged at 2000 rpm for 20 min to remove the excess PVP in the solution. Finally, the supernatant was discarded, and the pellet was redispersed with isopropyl alcohol for further use. Transition metal salts copper(II) chloride, manganese(II) chloride, iron(III) chloride, cobalt(II) chloride, chromium(III) chloride, and zinc chloride were used as oxygen scavengers, enabling the polyol synthesis of AgNWs under ambient air conditions. It was found that AgNWs synthesized in the presence of copper(II) chloride were approximately 36 μm long and approximately 90 nm in diameter, while reactions using other transition metal salts resulted in AgNWs with an average length of approximately 10 μm.

4.3. Results and Discussion

A schematic representation of the transition metal salt-promoted polyol synthesis of AgNWs in glycerol is shown in Figure 4.1. Glycerol used as a polyol compound acts as both solvent and reducing agent. $AgNO_3$ and PVP are silver precursor and stabilizing agents, respectively. Transition metal salts were used as oxygen scavengers. The whitish-gray colloidal appearance at the end of the reaction is a powerful indicator of nanowire formation. The morphology of the synthesized AgNWs was examined by the SEM. The reaction temperature during the synthesis plays an essential role in the final morphology of the nanowires. It was observed that high temperature speeds up the reaction rate. The reducing capability of glycerol can be attained by converting glycerol to glyceraldehyde at elevated temperatures. Consequently, silver ions can be reduced to metallic silver using aldehyde functional groups (-CHO) available in the glyceraldehydes.

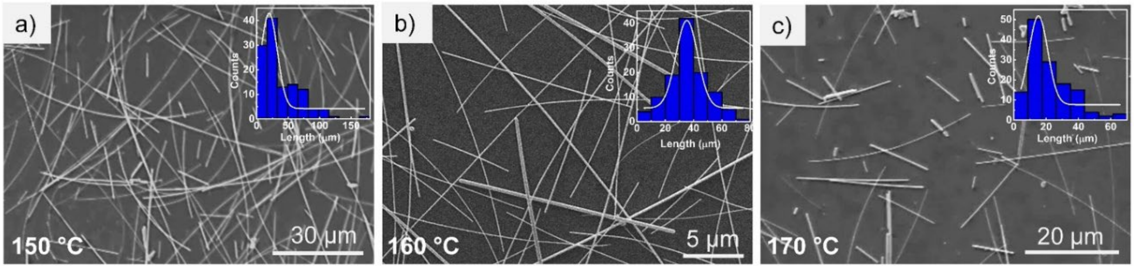

Figure 4.2. Effect of reaction temperature on the morphology of AgNWs. a) 150 °C, b) 160 °C, and c) 170 °C. The optimum reaction temperature for the polyol synthesis of AgNWs in Glycerol was determined to be 160 °C since the highest aspect ratio of AgNWs was obtained at this temperature.

Table 4.1. Effect of temperature on the morphology of AgNWs.

Temperature (°C)	Diameter (nm)	Length (μm)	Aspect Ratio
150	119 ± 60	38 ± 30	318
160	91 ± 21	36 ± 14	395
170	159 ± 68	22 ± 14	139

Figure 4.2 shows SEM images of AgNWs synthesized at 150, 160, and 170°C for a total reaction time of 120 min. The results shown in Figure 4.2 suggest that the aspect ratio of AgNWs and the reaction yield are strongly affected by the reaction temperature. At 150°C, the AgNWs were obtained with an average length of around 38 µm, while, at 160°C and 170°C, the average lengths of the AgNWs are smaller, 36 µm, and 22 µm, respectively. The average diameters of AgNWs grown at 170°C, 160°C, and 150°C are around 160 nm, 90 nm, and 120 nm, respectively. At 160°C, the highest aspect ratio of AgNWs was obtained, approximately 400 (Table 4.1). Therefore, the optimum reaction temperature for the polyol reaction in glycerol was determined to be 160°C since the highest aspect ratio and reaction yield were obtained at this temperature.

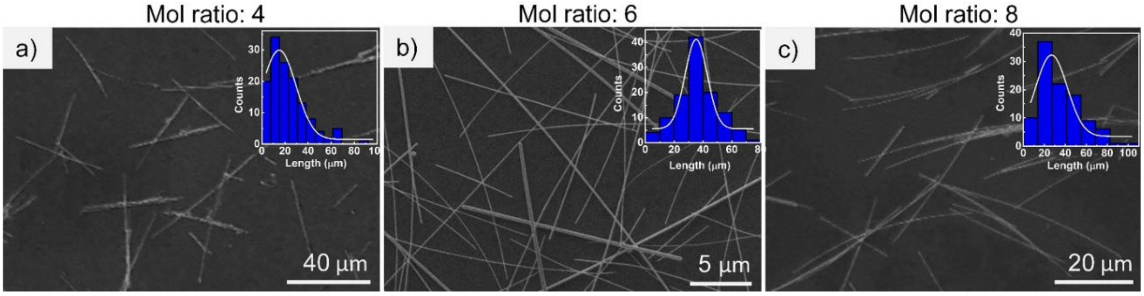

Figure 4.3. Effect of mole ratio of PVP/$AgNO_3$ on the morphology of AgNWs. The mole ratios of PVP/$AgNO_3$ are a) 4, b) 6, and c) 8. In the synthesis of AgNWs, the PVP/$AgNO_3$ mole ratio 6 generated the highest aspect ratio and yield. The reaction temperature of the reactions was held constant at 160 °C.

Table 4.2. Effect of PVP/$AgNO_3$ mole ratios of a) 4, b) 6, and c) 8 on the aspect ratios of AgNWs.

Mole Ratio of PVP/$AgNO_3$	Diameter of Ag NWs (nm)	Length of Ag NWs (µm)	Aspect Ratio of Ag NWs
4	233 ± 80	23 ± 16	99
6	91 ± 21	36 ± 14	395
8	186 ± 68	34 ± 20	184

The effect of the PVP: $AgNO_3$ mole ratio on the morphology and aspect ratio of the synthesized AgNWs were shown in Figure 4.3. It should be noted that PVP plays a vital role in polyol synthesis. PVP results in one-dimensional growth of nanowires by interacting with the {100} side surfaces of nanoparticles; hence, the deposition of silver is mainly preferred onto the {111} end surface, extending in one direction. Figure 4.3 shows SEM images of the AgNWs synthesized at varying PVP: $AgNO_3$ mole ratios of 4, 6, and 8. Notably, the reaction temperature was maintained at 160°C for all reactions. The average lengths of the AgNWs for the PVP: $AgNO_3$ mole ratios of 4, 6, and 8 are 23 µm, 36 µm, and 34 µm, respectively. The average diameters of the AgNWs are 233 nm, 91 nm, and 186 nm for the PVP, with $AgNO_3$ mole ratios of 4, 6, and 8, respectively. The longest and thinnest nanowires were obtained using the PVP: $AgNO_3$ mole ratio of 6 (Table 4.2). It should be noted that when the amount of PVP used in the synthesis is not enough for sufficient passivation of {100} faces of the seed nanoparticles, multi-twinned seed particles can grow on both {111} and {100} faces. When the mole ratio of PVP: $AgNO_3$ in the reaction mixture is 8, the excess PVP may cover all surfaces of the growing nanoparticles. Hence, elongation along {111} faces leading to anisotropic growth may be prevented. Therefore, using the PVP: $AgNO_3$ mole ratio 6, AgNWs were obtained with the highest aspect ratio.

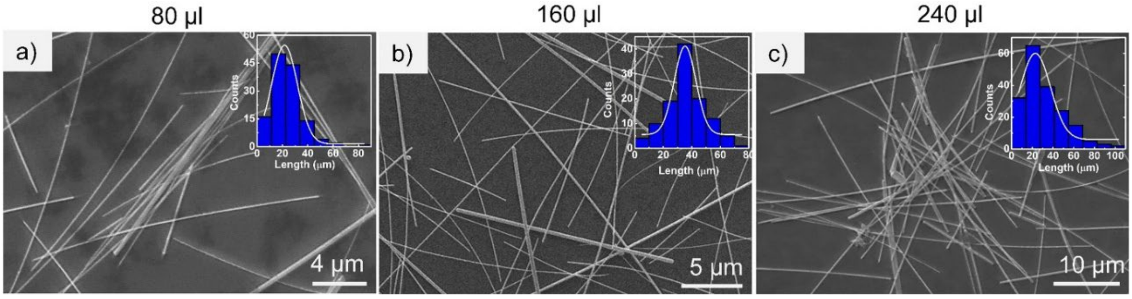

Figure 4.4. Effect of promoter amount on the morphology of AgNWs. The volume of the promoter (4 mM $CuCl_2$) is a) 80 µl, b) 160 µl, and c) 240 µl.

Table 4.3. Effect of transition metal salt ($CuCl_2$) amount on the aspect ratio of AgNWs.

Volume of 4 mM $CuCl_2$ (µl)	Diameter of Ag NWs (nm)	Length of Ag NWs (µm)	Aspect Ratio of Ag NWs
80	91 ± 32	24 ± 12	263
160	91 ± 21	36 ± 14	395
240	209 ± 79	32 ± 21	151

Another critical parameter strongly affecting the morphology of the AgNWs is the amount of promoter used in the polyol synthesis of nanowires. It should be noted that the reaction temperature was kept constant at 160°C, and 4 mM $CuCl_2$ was used as a promoter for the reactions discussed in this section. SEM images of the AgNWs synthesized with varying volumes of 4 mM $CuCl_2$ solution (0.080 mL, 0.160 mL, and 0.240 mL) are shown in Figure 4.4. The average lengths of the AgNWs obtained from the reaction mixture containing 0.080 mL, 0.160 mL, and 0.240 mL of 4 mM $CuCl_2$ are 24 μm, 36 μm, and 32 μm, respectively, while the average diameters of AgNWs are 91 nm, 91 nm, and 209 nm, respectively. The results suggest that the highest aspect ratio of around 400 was obtained from AgNWs synthesized using 0.160 mL of 4 mM $CuCl_2$ (Table 4.3).

Furthermore, the reaction yields of 0.080 and 0.160 mL of 4 mM of $CuCl_2$ are higher than those of 0.240 mL of 4 mM of $CuCl_2$. Therefore, the optimum amount of transition metal salt promoter in the polyol synthesis of AgNWs in glycerol was determined to be 0.160 mL of 4 mM $CuCl_2$.

Additionally, we have extensively studied the effect of some transition metal salts as promoters on the morphology of AgNWs. The experimental results suggest that transition metal salts are stringently required to synthesize AgNWs in an open atmosphere. In this study, several types of transition metal salts, such as $CuCl_2$, $CoCl_2$, $MnCl_2$, $CrCl_3$, $FeCl_3$, and $ZnCl_2$, have been investigated as promoters in the polyol synthesis of AgNWs in glycerol (Figure 4.5). The results presented in Figure 4.5a indicate that AgNWs synthesized in the presence of $CuCl_2$ have the longest length. The average lengths of AgNWs in the presence of $CoCl_2$, $ZnCl_2$, $CrCl_3$, $FeCl_3$, $MnCl_2$, and $CuCl_2$ were 7, 10, 10, 11, 12, and 36 μm, respectively (Table 4.4). Concurrently, the average diameters of the AgNWs in the presence of $CoCl_2$, $ZnCl_2$, $CrCl_3$, $FeCl_3$, $MnCl_2$, and $CuCl_2$ are 77, 74, 50, 230, 67, and 91 nm, respectively. The thinnest and the most uniform nanowires are grown in the presence of $CrCl_3$.

Nevertheless, the results suggest that the highest aspect ratio of AgNWs was achieved when $CuCl_2$ was used as a promoter in the synthesis. Therefore, $CuCl_2$ was the optimum transition metal salt promoter in the polyol synthesis of AgNWs in glycerol. The experiment was also performed under the optimized reaction conditions without using a transition metal salt promoter in glycerol. However, in these control experiments, we observed many Ag nanoparticles and only a few short AgNWs (Figure 4.6). The halide ions such as Cl^- provided by the dissociation of transition metal salts in water may effectively react with the free silver ions, and thus they form AgCl complexes.[67] Also note that thermodynamically stable multi-twinned seed nanoparticles, provided by the slow and controlled reduction of silver ions, are required to synthesize silver nanowires with high yield and high aspect ratio.[68] However, oxygen molecules in the air can quickly adsorb and dissociate into atomic oxygen on these seed nanoparticle surfaces. In an open atmosphere synthesis of AgNWs, the atomic oxygen could cover the surface of silver seed nanoparticles, and hence, the atomic oxygen blocks the growth of AgNWs.[69] However, in the presence of transition metal ions during the open atmosphere synthesis of AgNWs, transition metal ions can scavenge adsorbed atomic oxygens from the silver seeds; therefore, AgNWs can easily grow in the open atmosphere.[68] In our study, the observed effect of several transition metal salts may be due to their different oxygen scavenging capability.

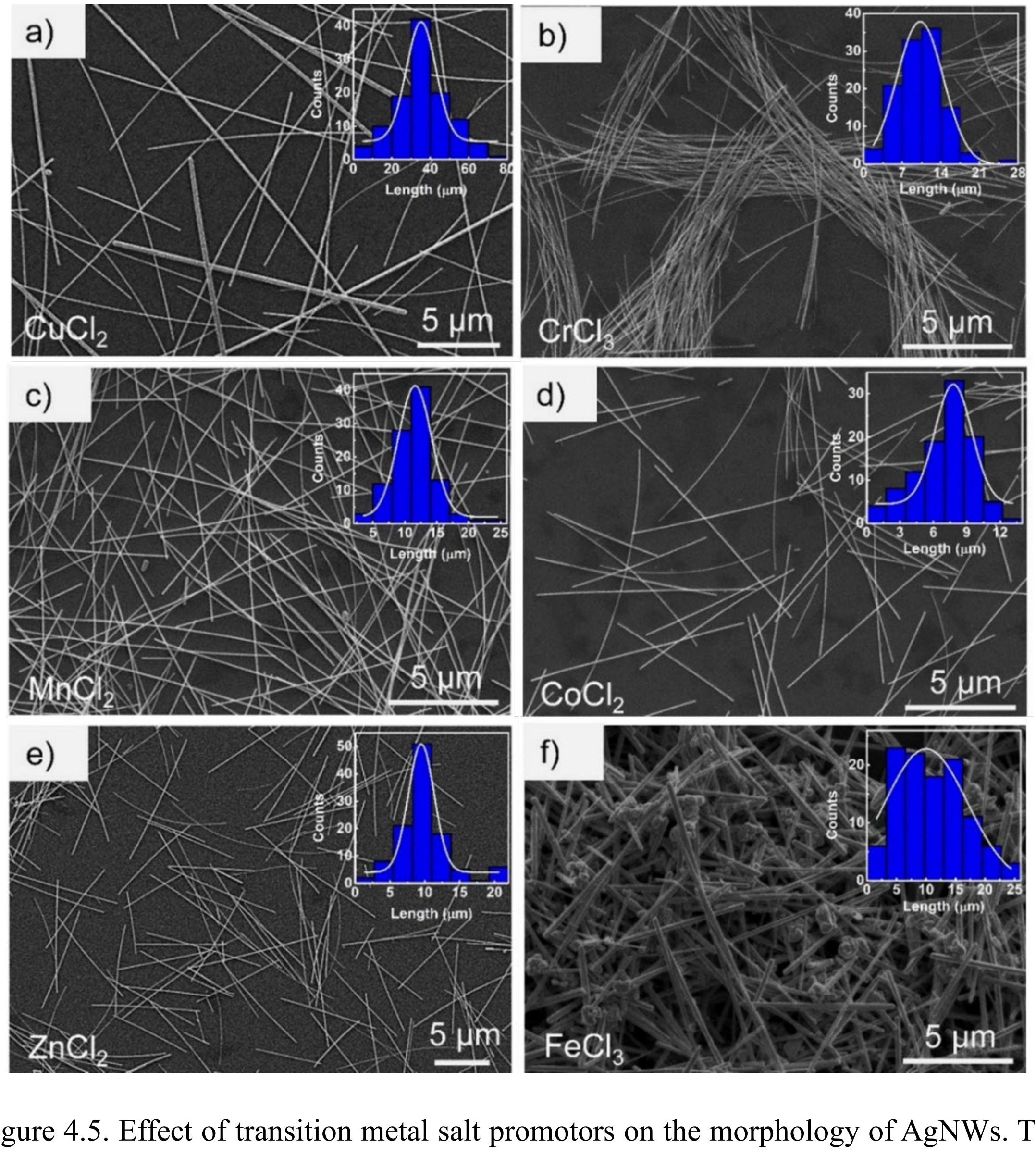

Figure 4.5. Effect of transition metal salt promotors on the morphology of AgNWs. The promotors used for the synthesis of AgNWs are a) $CuCl_2$, b) $CrCl_3$, c) $MnCl_2$, d) $CoCl_2$, e) $ZnCl_2$, and f) $FeCl_3$. The nanowires synthesized using $CuCl_2$ as a promoter exhibit the highest aspect ratio.

Table 4.4. Effect of transition metal salts used as promoters in polyol synthesis of AgNWs in glycerol on the aspect ratio of AgNWs.

Transition Metal Salt	Diameter of Ag NWs (nm)	Length of Ag NWs (μm)	Aspect Ratio of Ag NWs
$CuCl_2$	91 ± 21	36 ± 14	395
$CrCl_3$	50 ± 10	10 ± 4	202
$MnCl_2$	67 ± 9	11 ± 4	170
$CoCl_2$	76 ± 12	7 ± 3	92
$ZnCl_2$	74 ± 15	10 ± 4	133
$FeCl_3$	230 ± 53	11 ± 6	48

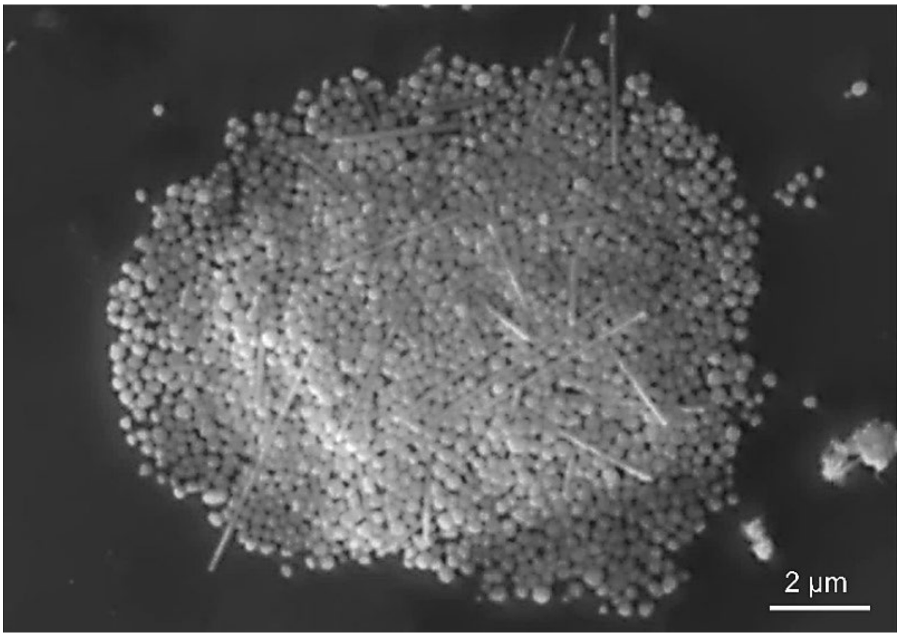

Figure 4.6. An SEM image of the reaction products obtained under the optimized reaction conditions from the polyol reduction of silver ions in the absence of transition metal salt promoters.

To determine the optimum reaction time and stirring condition and understand the growth mechanism of nanowires, experimental extinction spectra of AgNWs were obtained after adding silver precursor. Aliquots were taken at selected times from the reaction at 160 °C in the presence of $MnCl_2$ as a promoter and monitored serially using broadband absorption spectroscopy. Figure 4.7 and Figure 4.8 show the time evolution of extinction spectra of the reaction mixture and the SEM images, respectively. AgNWs have two main plasmon polariton resonance modes: the longitudinal plasmon polariton mode (along the main axis of the nanowire) and the transverse plasmon polariton mode (in the plane perpendicular to the main axis of the nanowire). After 5 minutes of the first addition of $AgNO_3$, the extinction spectrum shows a resonance peak at around 410 nm, most probably due to the localized surface plasmon polariton formation of nearly spherical silver nanoparticles, as also supported by SEM observations. As the reaction proceeds, the optical density of AgNWs increases since the concentration of AgNWs increases with time. The appearance of a sharp extinction peak at around 380 nm is a strong indication of AgNWs formation.[61]

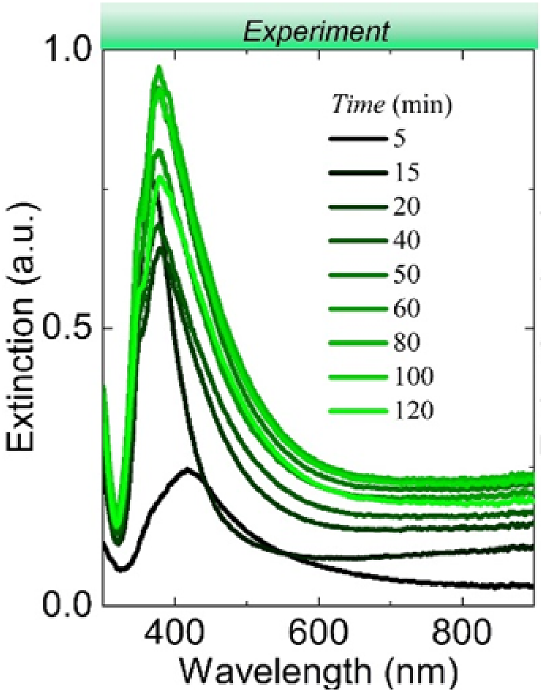

Figure 4.7. Time evolution of the extinction spectra of AgNWs. UV-Vis spectra of reaction products during the growth of AgNWs in the presence of $MnCl_2$ as a promoter.

The results indicate that the nanowire formation starts around 10 min after adding $AgNO_3$ to the reaction medium. At the end of the reaction (around 120 min after the first addition of $AgNO_3$), AgNWs have an average length of 12 μm and an average diameter of 67 nm. In contrast, the concentration of Ag nanoparticles is significantly reduced. Therefore, the optimum reaction time was determined to be 120 min. The effect of stirring conditions on the morphology of AgNWs was investigated using 160 μL of 4 mM $CuCl_2$ as the promoter, a PVP: $AgNO_3$ molar ratio of 6, and a temperature of 160 °C. For the unstirred condition, the stirring speed of the reaction mixture was reduced to zero immediately after the dropwise addition of $AgNO_3$ (Figure 4.8).

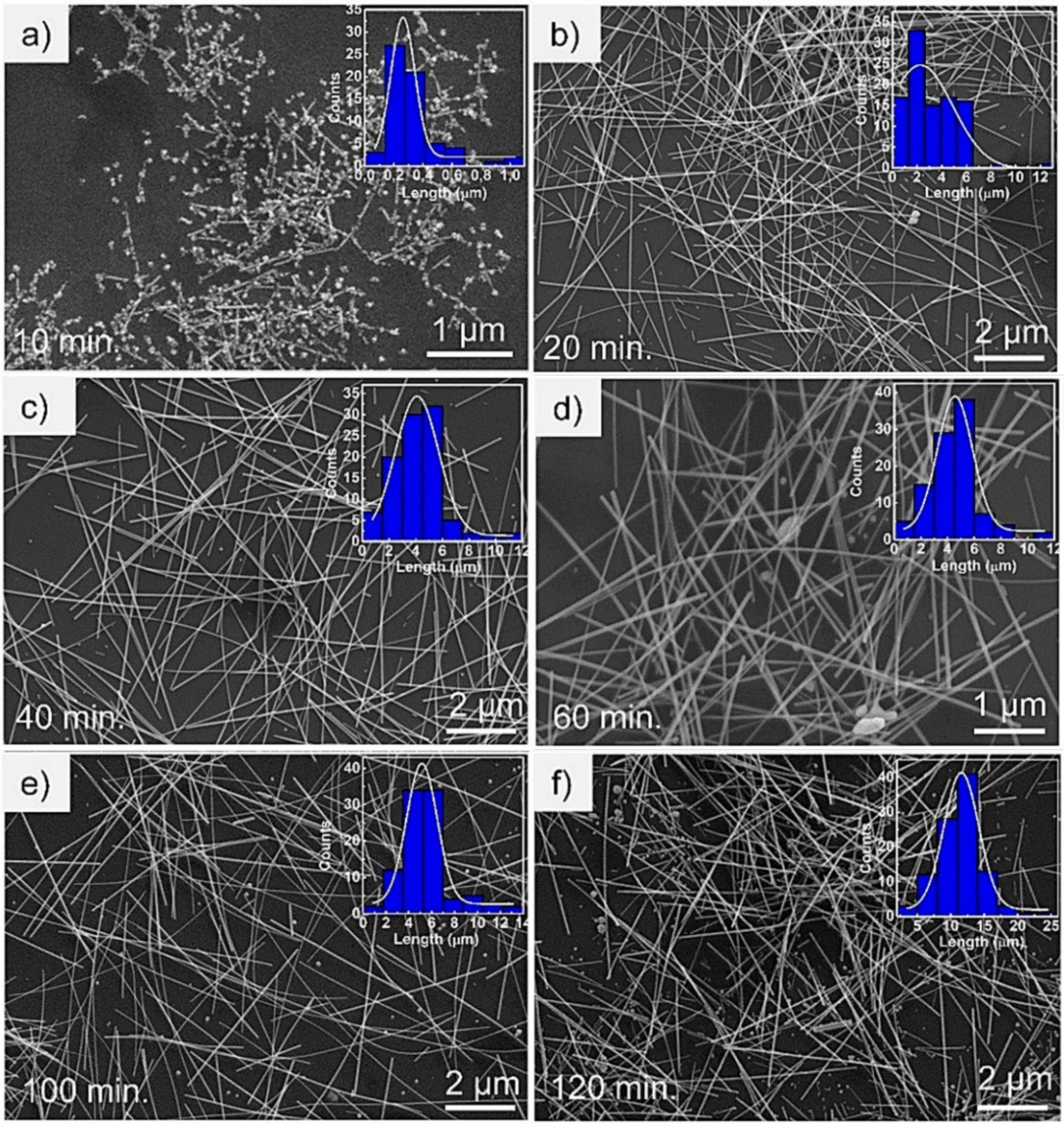

Figure 4.8. SEM images of the reaction products were taken after (a) 10 min, (b) 20 min, (c) 40 min, (d) 60 min, (e) 100 min, and (f) 120 min in the presence of $MnCl_2$ as a promoter during the growth.

The length, diameter, and aspect ratio of the AgNWs obtained under various reaction conditions are given in Table 4.5. Notably, the length and diameter of AgNWs increased when the reaction was not stirred, as the chance of silver atoms accumulating on the silver nanowires and seed nanoparticles increased.

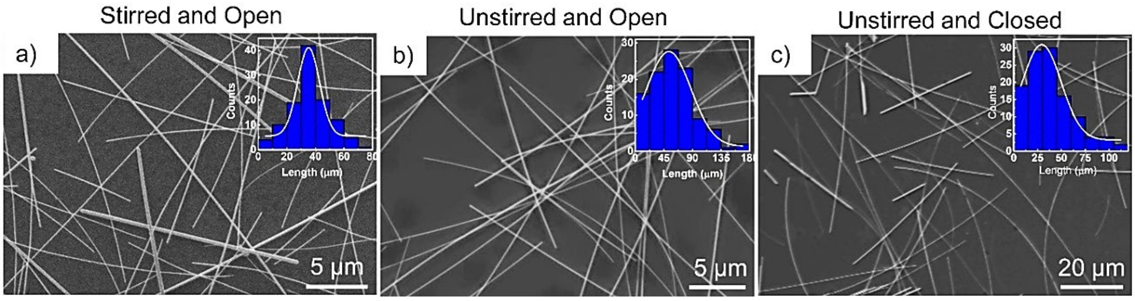

Figure 4.9. Effect of stirring during the polyol synthesis of nanowires in glycerol on the morphology of AgNWs. The synthesis of AgNWs was performed a) under stirring at 200 rpm, b) without stirring, and the reaction vessel was open, and c) without stirring, and the reaction vessel was closed. In (c), the reaction vessel was hermetically closed, preventing air passage.

Table 4.5. Effect of reaction condition on the aspect ratio of AgNWs.

Reaction Condition	Diameter of Ag NWs (nm)	Length of Ag NWs (μm)	Aspect Ratio of Ag NWs
Stirred and Open Air Atmosphere	91 ± 21	36 ± 14	395
Unstirred and Open Air Atmosphere	133 ± 31	60 ± 34	451
Unstirred and Closed Air Atmosphere	151 ± 83	39 ± 25	258

4.4. Conclusion

In conclusion, for the first time, we have demonstrated a facile, green, high yield, transition metal salt promoted, and open atmosphere method for synthesizing high-quality AgNWs in an environmentally benign solvent, a glycerol-water mixture. It was shown that various transition metal salts strongly influence the shape and size of the AgNWs produced by the polyol reduction of $AgNO_3$. In the presence of transition metal salts, the transition metal removes oxygen from the silver seeds' surfaces, allowing the silver nanoparticles to grow in one direction. The effect of several reaction parameters such as temperature, mole ratio of PVP: $AgNO_3$, type of promoter, amount of promoter, reaction time, and stirring condition on the morphology of AgNWs were extensively studied. Under the optimized reaction conditions, AgNWs with a high aspect ratio of more than around 400 were obtained by using $CuCl_2$ as a promoter.

CHAPTER 5

IRON OXIDE NANOCUBE ASSEMBLY ON SILVER NANOWIRE TEMPLATES TO ENHANCE MAGNETIC HYPERTHERMIA PERFORMANCE

5.1. Introduction

Magnetic hyperthermia therapy (MHT) is a promising cancer treatment approach that uses magnetic nanoparticles to generate heat inside tumors.[45] The nanoparticles delivered to the tumor site dissipate heat under an externally applied AC magnetic field, which increases the temperature (42-46°C) in the tumor site, destroying cancer cells. The heating performance of the magnetic nanoparticles is expressed with a specific absorption rate (SAR). The SAR should be as high as possible to minimize the particles required for MHT and keep the applied magnetic field within clinically acceptable levels.[40] Magnetic nanoparticles' dynamic magnetization response is the basis for calculating SAR. The effective magnetic anisotropy of nanoparticles, as well as the frequency and amplitude of the external magnetic field applied to the material, affect the SAR value by changing the hysteresis loop shape and area (i.e., dynamic magnetization response). Therefore, increasing the saturation magnetization (M_s) and coercive field (H_c) of the nanostructure is predicted to enhance the SAR.

Effective magnetic anisotropy is a measure of a material's resistance to magnetization and is responsible for the shape of the hysteresis loop.[70] It is influenced by factors of magnetocrystalline anisotropy, shape anisotropy, surface anisotropy, and interparticle interactions. Tuning is one of these factors that may contribute to an increase in SAR. For instance, theoretical and experimental studies have demonstrated that cubic iron oxide nanoparticles (IONCs) exhibit higher SAR than spherical ones. This is attributed to their reduced number of facets and lower level of disordered spin.[42] In another study, SAR values of various nanostructures were presented by ranking them from highest to lowest, with nanocubes being the most effective, followed by nanoflowers, nanooctahedra, and nanorods.[45] Another approach to increase SAR is to arrange nanoparticles in a chain-like or columnar structure, enabling dipolar coupling.[42]

The dipolar coupling may cause difficulties for nanostructures in rotating their magnetization direction, which increases the coercivity of the system, leading to higher hysteresis losses and, ultimately, greater heat generation. The discovery of the heating performance of magnetotactic bacteria-synthesized magnetosome chains and the observation that magnetic nanoparticles in a fluid tend to form linear clusters under a uniform magnetic field sparked interest in this approach.[7] However, it should be noted that the effect of the tendency to form linear clusters under a magnetic field can be disrupted when the magnetic field is removed unless the particles are fixed in a matrix. Additionally, attempting to achieve random chain formation via high particle concentration may lead to aggregation, resulting in lower SAR values.[71]

Silver nanowires (AgNWs) have attracted significant attention due to their superior conductivity, flexibility, and transparency. Their applications in electronics, photonics, energy storage, and biomedical fields are extensively researched. The most common applications are transparent conductive films, sensors, substrates for surface plasmon resonance sensors, batteries, drug delivery, and antimicrobial applications. Furthermore, the high aspect ratio of AgNWs enables them to serve as a unique template for synthesizing 1D nanoparticles with novel structures and functions.[72]

Here, a new approach is presented that enables the formation of chain-like structures to improve the SAR values of IONCs. The high aspect ratio and surface area of AgNWs were used as a template to obtain chain-like structures composed of IONCs. Thus, the magnetic anisotropy of IONCs, known for their high heating efficiency due to their shape anisotropy, was increased further to enhance the SAR. For this, IONCs were synthesized by solvothermal methods. Their surfaces were functionalized by post-synthesis and attached to the surface of AgNWs via electrostatic forces. The heating efficiency of the nanostructures was investigated by AC magnetometry under various frequencies (i.e., 110, 200, and 300 kHz) and magnetic field strength (i.e., 12, 16, and 24 $kA.m^{-1}$) at a constant temperature of 20°C. It has been evaluated that chain-like structures promote dipolar coupling at a magnetic field strength of 24 $kA.m^{-1}$, regardless of applied frequency.

5.2. Materials and Methods

Iron(0) pentacarbonyl (>99.99% trace metal bases), 1-octanol (anhydrous, ≥99%), oleic acid (≥99%, G.C.), benzaldehyde (≥99%, ReagentPlus), ethyl acetate (ACS reagent,

≥99.5%) acetonitrile (≥99.9%), chloroform, acetone, toluene, ethanol (ACS reagent, ≥99.5%) were purchased from Sigma-Aldrich. Polyethyleneimine (branched, M.W. 10,000, 99%, Alfa Aesar) was purchased from Thermo Fisher Scientific. All chemicals were used as received without further purification. Milli-Q water with 18.2 MΩ·cm electrical resistivity was used.

The synthesis of AgNWs was conducted as described previously by our group.[73] The method includes Glycerol as polyol solvent, silver nitrate ($AgNO_3$) as the silver source, polyvinylpyrrolidone (PVP, M_w ~1,300,000) as stabilizing agent, and iron(III) chloride hexahydrate ($FeCl_3.6H_2O$) as promoters. In the synthesis, 5.0 mL of glycerol is heated to 160°C in a glass vial and stirred for 2 h under 200 rpm magnetic stirring. Then, 4 mM transition metal salt is added to the vial. After that, 0.1 M $AgNO_3$ and 0.6 M PVP dissolved in the glycerol-water mixture solvent were added to the hot glycerol solution. Subsequently, the magnetic stirrer was removed, and the reaction solution was left at 160°C for another 2 h. The reaction was ended by quenching a glass vial into the ice-water bath. The synthesized AgNWs were purified to remove the by-products formed along with the AgNWs using the anti-solvent method with acetone.

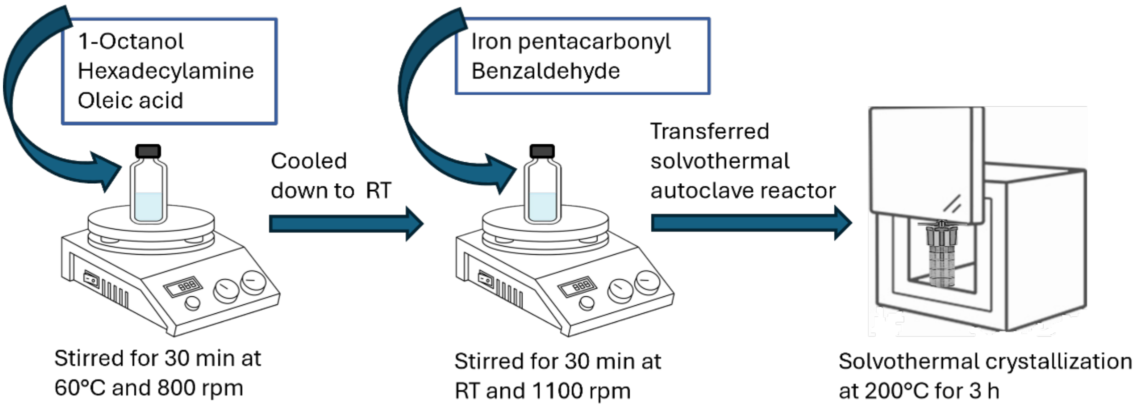

Figure 5.1. Schematic representation of the solvothermal synthesis of iron oxide nanocubes.

IONCs were synthesized via the solvothermal method (Figure 5.1), as reported in the work of Gavilán et al.[52] In the synthesis, 1-octanol was used as the solvent, iron pentacarbonyl as the metal source, oleic acid as the stabilizing agent, benzaldehyde as the shape-guiding agent, and hexadecylamine as the shape-adjusting agent. Firstly, the homogenous solution of 1-octanol (8.0 mL), hexadecylamine (0.2 g), and oleic acid (0.6 mL) was prepared into a glass vial under 800 rpm magnetic stirring at 60°C for 30 min.

After that, the solution was cooled to room temperature (RT), 2.0 mL of iron pentacarbonyl and 1.0 mL of benzaldehyde were added and stirred under 1100 rpm at RT for 30 min. Then, the prepared solution was transferred to the 25.0 mL solvothermal autoclave reactor with a 46% filling rate. The autoclave reactor was placed in the oven at 200°C and left for 3 h. End of the reaction time, the autoclave was removed from the oven and allowed to cool to ambient temperature. After that, the particles were dispersed and stored in chloroform.

The surface of the as-synthesized IONCs is hydrophobic due to the oleic acid molecules on their surfaces. Their surfaces were functionalized with PEI to make the IONCs dispersible in water without agglomeration and decorate them on the AgNWs. In this procedure, the surface of the IONCs was conjugated with PEI, which is widely used in biomedical applications.[7475,76] The representative chemical mechanism of PEI coating is shown in Figure 5.2.

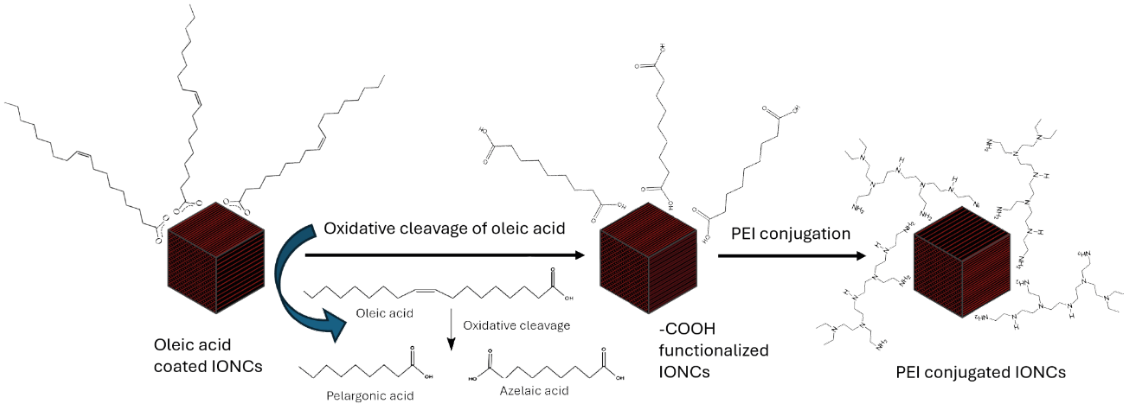

Figure 5.2. Representative chemical step of the PEI coating procedure.

The schematic of the experimental procedure for the PEI coating of IONCs surfaces is given in Figure 5.3. In the experimental procedure, 0.5 mL of IONCs in $CHCl_3$ was put in a centrifuge tube, and 1.5 mL of acetone was added. This solution was vortexed for 10 sec. and centrifuged at 1500 rpm for 5 min. At the end of the centrifuge, the supernatant of the solution was discarded, and IONCs precipitates were dried with N_2 and redispersed in 0.5 mL toluene. Then, 0.1 mL ethyl acetate and 0.1 mL acetonitrile were mixed in a glass bottle, and a precise amount of IONCs solution in toluene was added to this mixture. After that, 0.28 M sodium periodate solution was prepared in water, and 0.15 mL of it was added to the solution as an oxidizing agent. The solution was sonicated in the ultrasonic bath for 20 min by keeping the temperature between 30-35°C at 45 kHz. At the end of the sonication, IONCs particles were separated magnetically, and the supernatant was discarded. The precipitate was washed with ethanol twice and then washed with distilled water three times to remove excessive reactants by magnetic seperation. At the end of this step, the hydrophilic IONCs functionalized with the -COOH group were obtained and coded as IONCs@COOH. To conjugate IONCs@COOH surfaces with PEI, first, PEI is dissolved in water at 20 mg.mL^{-1} concentration. Then, 0.25 mL of IONCs@COOH solution was added to 20 mL of PEI solution dropwise under sonication. This solution was sonicated for a further 3 h in the ultrasonic bath. After that, the solution was washed five times with water by membrane-filtered centrifuge tubes (Amicon membrane filters of 100K MWCO), redispersed in water, and sonicated with a probe sonicator at 45 kHz for 10 min. These samples are named as IONCs@PEI.

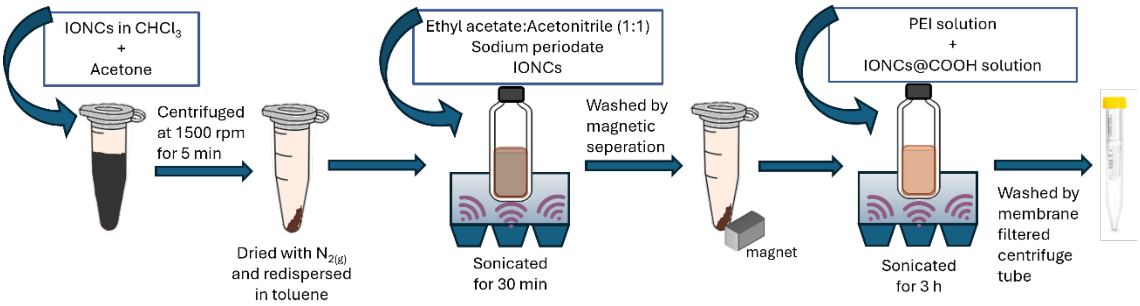

Figure 5.3. The schematic of the experimental procedure of surface functionalization of IONCs with PEI.

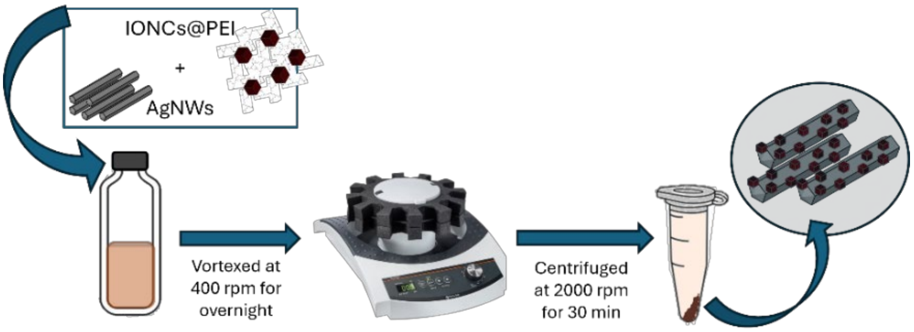

Figure 5.4. Schematic representation of the preparation of magneto-plasmonic nanoparticles from IONCs@PEI particles.

For the decoration of IONCs@PEI on the AgNWs, 5.0 mL of concentrated IONCs@PEI solution was prepared in a glass vial and placed in a vortex shaker (multi-reax vortex shaker, Heidolph) (Figure 5.4). Then, 0.5 mL AgNWs colloidal solution was added to the IONCs@PEI solution at 400 rpm and left for several hours. The IONCs@PEI attached AgNWs samples named as AgNWs@IONCs@PEI. After that, to remove non-attached IONCs@PEI nanoparticles, the mixture was centrifuged at 2000 rpm for 30 min. This step was repeated two times, and the final precipitates of AgNWs@IONCs@PEI were dispersed in water.

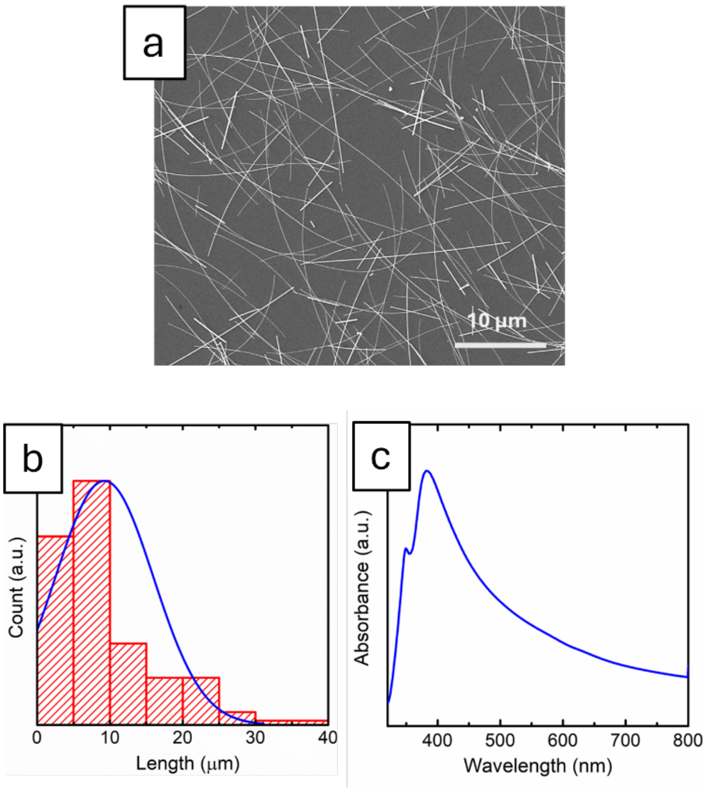

Figure 5.5. The SEM image (a), length size distribution graph (b), and the absorption spectrum of the AgNWs.

A scanning electron microscope (SEM) image of the AgNWs sample was taken using a JEOL JSM-6490LA instrument at 10 kV acceleration voltage using a secondary electron detector. Transmission electron microscopy (TEM) analysis was performed to observe the nanoparticles' size and morphology and the assembled structure of IONCs on AgNWs using the JEOL JEM-1400 microscope at an accelerating voltage of 120 kV. To prepare TEM samples, diluted nanoparticle solutions were dropped onto 200 mesh carbon-coated copper grids. The particle size and size distribution of AgNWs and IONCs samples were calculated using ImageJ software from the electron microscopy images. The hydrodynamic size (d_h), size distribution, and surface zeta potential measurement of the nanoparticles were conducted by dynamic light scattering (DLS) using a Zetasizer (Nano ZS90, Malvern, U.K.) instrument. All DLS measurements were repeated three times. The pH value of the reaction medium was measured with pH indicator papers. Ultraviolet-visible spectroscopy (UV-Vis) characterization was carried out to confirm that AgNWs were synthesized. The surface chemistry of the nanoparticles was analyzed by Fourier transform infrared spectroscopy with an attenuated total reflectance configuration (ATR-FTIR) using a Vertex 70V Bruker instrument. The XRD pattern of the nanoparticles was realized using a PANalytical Empyrean X-ray diffractometer equipped with a 1.8 kW Cu Kα ceramic X-ray tube and a PIXcel3D 2×2 area detector operating at 45 kV and 40 mA. For XRD, concentrated nanoparticle solutions were dropped onto a zero-diffraction quartz wafer. Inductively coupled plasma optical emission spectroscopy (ICP-OES, ThermoFisher CAP 6000 series) was used for the elemental analysis. To carry out ICP-OES analysis, 0.01 mL of nanoparticle solution was added to 1.0 mL of aqua regia and left overnight for digestion. The sample solution was then diluted to 10.0 mL by adding Milli-Q water and filtered through a 0.45μm PTFE membrane. AC magnetometer (AC Hyster advance, Nanotech solutions) was used to reveal the dynamic magnetization curves of the hydrophilic magnetic nanoparticles under the frequencies of 110, 200, and 300 kHz, applying 12, 16, and 24 $kA.m^{-1}$ magnetic fields at 20°C. AC magnetometer measurements were repeated three times for each set of samples and conditions.

5.3. Results and Discussion

SEM images of the AgNWs sample and length size distribution graph are given in Figure 5.5 a and b. The length and diameter size distributions of the AgNWs sample were found to be 9±7 µm and 109±27 nm using ImageJ software. The UV-Vis spectrum of the synthesized AgNWs samples is given in Figure 5.5 c. The appearance of the peak observed at approximately 350 nm is indicative of AgNWs formation.

TEM images and particle size distributions of IONCs are given in Figure 5.6 a and d, respectively. The mean particle size distribution of IONCs was 15±1 nm. Also, the concentration of the Fe ions was analyzed by the ICP-OES and found to be 3.2 $mg.mL^{-1}$.

The agglomeration-free particle formation for IONCs@COOH and IONCs@PEI samples was shown in Figures 5.6 c and d by TEM analysis, respectively. Hydrodynamic size measurements of samples by intensity and number measured by DLS exhibited unimodal size distribution (Figure 5.6 e and f). Hydrodynamic size distribution by intensities was measured as 49±23 and 90±38 nm and by numbers 21±7 and 43±14 nm with 0.197 and 0.186 PDI values for IONCs@COOH and IONCs@PEI samples, respectively. The zeta potential distribution of IONCs@COOH and IONCs@PEI were measured as -15.4±11.4 and 36.1±12.4 mV, respectively.

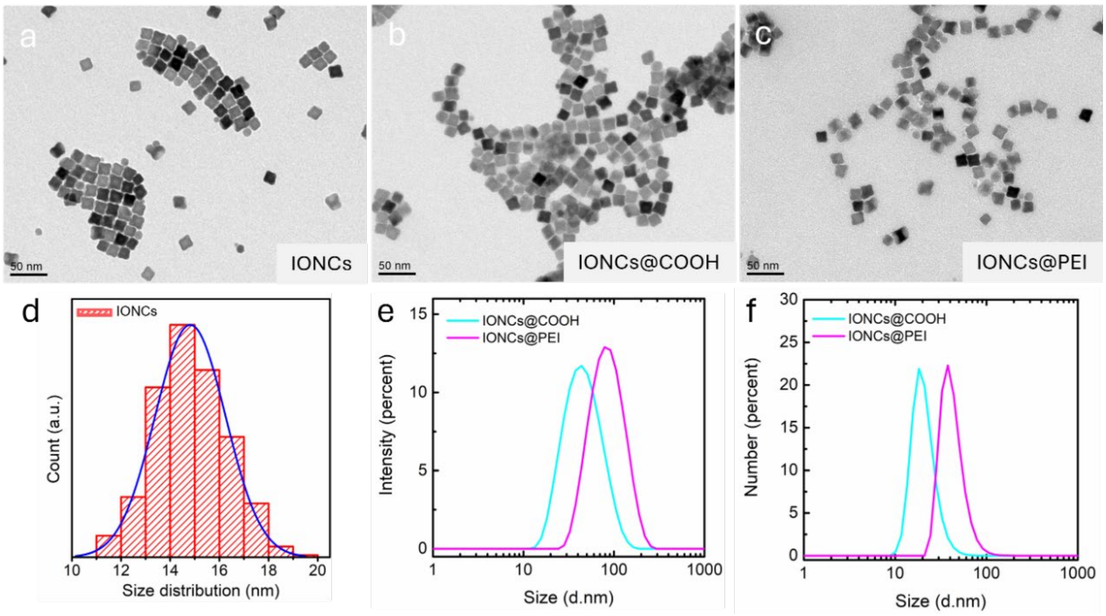

Figure 5.6. The TEM images (a, b, c), the particle size distribution of IONCs (d), and the hydrodynamic particle size distribution graphs of IONCs@COOH and IONCs@PEI samples by intensity (e) and number (f).

Schematic representations of functional groups on the surface of the IONCs, ATR-FTIR spectrum, and XRD pattern of the IONCs, IONCs@COOH, and IONCs@PEI samples are given in Figure 5.7 a, b, and c, respectively. The peak intensity of the IONCs@COOH FTIR spectrum is lower due to the use of different ATR-FTIR instruments (Perkin Elmer– UATR TW). For the IONCs@COOH, the broad absorption peak between 3500-3000 cm^{-1} can be attributed to the O-H stretching vibration of the carboxylic acid group. The peaks at 1629 and 1397 are assigned to C=O stretching vibration and CH_2 bending vibrations, respectively. The broadband seen in the spectrum of IONCs@PEI between 3400-3200 cm^{-1} is attributed to N-H stretching vibrations of primary and secondary amines. The 2934 and 2848 cm^{-1} peaks are associated with C-H stretching vibrations of methylene groups. The weak to medium peaks observed between 1600-1500 cm^{-1} were assigned to N-H bending vibrations. The absorption peaks at 1476, 1300, and 1033 cm^{-1} frequencies were attributed to C-N stretching vibrations. The XRD patterns showed that all samples had the same diffraction peaks, which are well-matched with the magnetite phase of iron oxide (Fe_3O_4) with the ICDD card number 75-0033. Analysis revealed that the crystal phase of the particles was preserved during the surface functionalization steps.

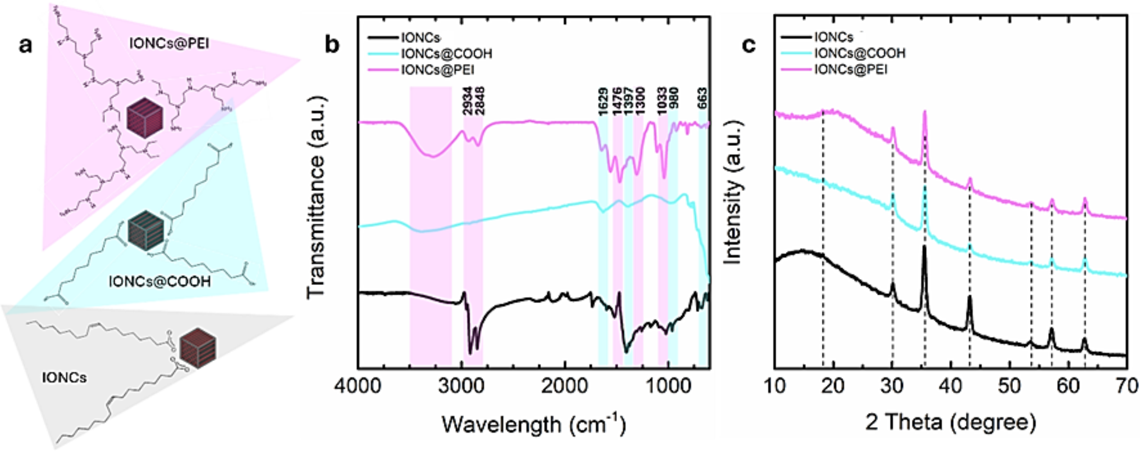

Figure 5.7. The representative surface functional group schematic and corresponding ATR-FTIR spectrum (b) and XRD pattern (c) of IONCs, IONCs@COOH, and IONCs@PEI.

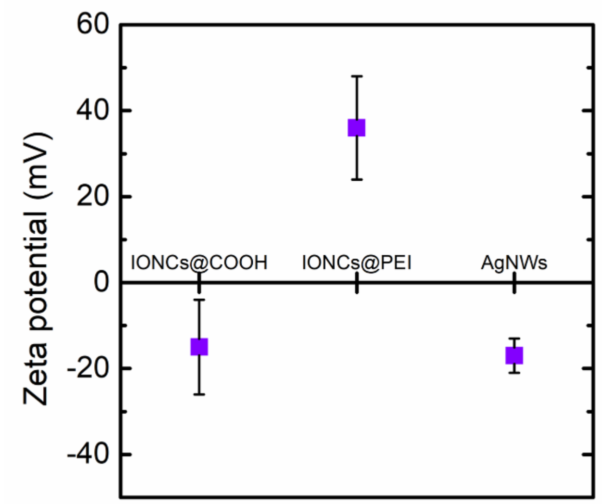

Sample name	Zeta potential (mV)	Std. dev.
IONCs@COOH	-15.4	11.4
IONCs@PEI	36.1	12.4
AgNWs	-16.5	4

Figure 5.8. Zeta potential graph and values of IONCs@COOH, IONCs@PEI, and AgNWs.

The surface zeta potential of IONCs@COOH, IONCs@PEI, and AgNWs were measured in water around a pH of 6-7 with pH indicator papers at 20°C (Figure 5.8). The surfaces of IONCs@PEI were positively charged, while the AgNWs' surfaces were negatively charged due to the presence of PEI and PVP on their surface, respectively. Figure 5.9 shows the TEM images of AgNWs@IONCs@PEI particles at various magnifications. Neither entanglement of AgNW nor agglomeration of IONCs@PEI were observed. The distribution of IONCs@PEI on the PVP-stabilized AgNWs surface was primarily homogeneous but not in a perfect chain-like structure. The stable deposition of IONCs@PEI nanoparticles onto AgNWs was primarily due to the electrostatic attraction due to the opposite surface zeta potentials, accompanied by van der Waals forces.

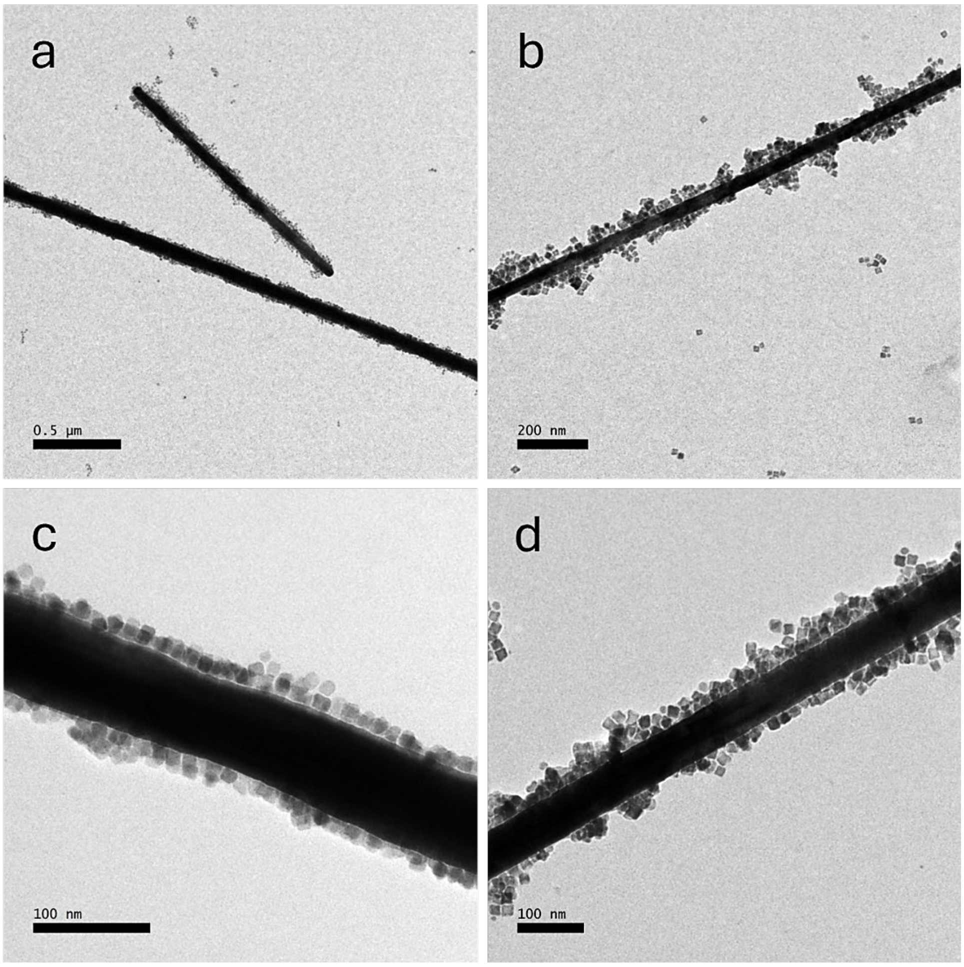

Figure 5.9. TEM images at various magnifications of AgNWs@IONCs@PEI.

The dynamic hysteresis loops of the hydrophilic magnetic nanoparticles were evaluated using AC magnetometry under various frequencies and magnetic fields. The valuable data about the magnetic properties of nanoparticles can be determined from the hysteresis loop, such as coercive field (H_c), saturation magnetization (M_s), remanence (M_r), critical magnetic field (H_{cr}), and susceptibility (χ). These data can provide information about magnetic interactions and possible arrangements of nanoparticles.

The applied field conditions stretched beyond the Brezovich limit ($H_{AC} . f \leq 5 \times 10^9 A.m^{-1}.s^{-1}$), which defines the clinically suitable value of magnetic hyperthermia therapy for the proof of concept study. In this study, maximum applied field conditions (i.e., 300 kHz and 24 $kA.m^{-1}$) corresponds to approximately 7.2 $\times 10^9 A.m^{-1}.s^{-1}$ The iron concentration of the IONCs@COOH and IONCs@PEI samples used in the AC magnetometer measurement was 0.6 $mg.mL^{-1}$, while the iron concentration of the AgNWs@IONCs@PEI sample was 0.15 $mg.mL^{-1}$.

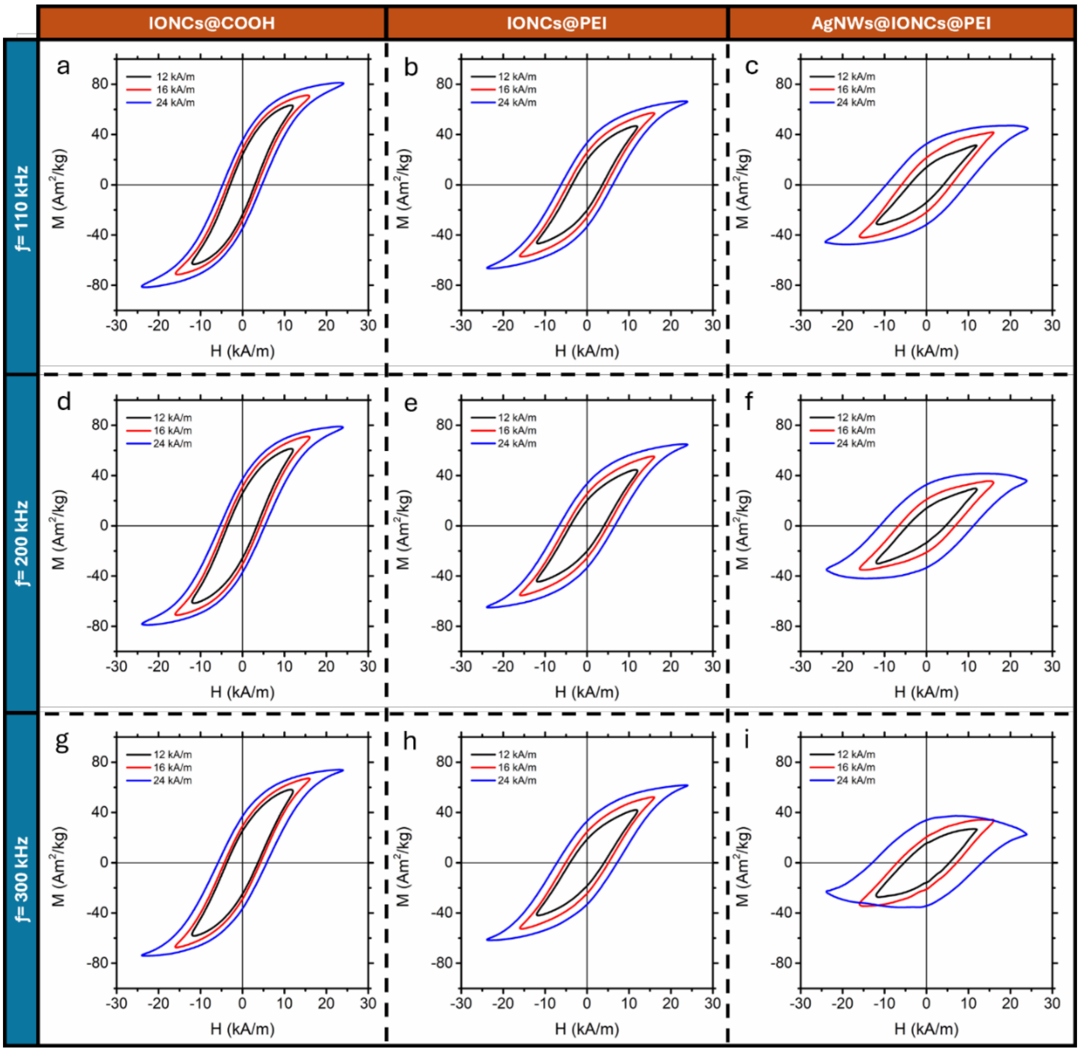

Figure 5.10. AC hysteresis loops of IONCs@COOH (a, d, g), IONCs@PEI (b, e, h), and AgNWs@IONCs@PEI (c, f, i) under various frequencies and magnetic field strength.

Table 5.1. Dynamic magnetic properties of IONCs@COOH, IONCs@PEI, and AgNWs@IONCs@PEI.

Sample Name	**H_{app} (kA.m^{-1})**	**H_c (kA.m^{-1})**	**M_s (Am^2.kg^{-1})**	**M_r (Am^2.kg^{-1})**	**M_r/M_s**	**Area (mJ.kg^{-1})**	**SAR (W.g^{-1})**
110 kHz							
IONCs@COOH	12	2.9±0.0	63.3±0.1	23.8±0.2	0.38	811±6	89±1
	16	3.6±0.0	71.3±0.4	28.3±0.3	0.40	1145±14	126±2
	24	4.7±0.1	81.4±0.5	35.0±0.3	0.43	1804±40	198±4
IONCs@PEI	12	3.6±0.0	46.8±0.3	20.0±0.2	0.43	698±8	77±1
	16	4.6±0.0	57.2±0.3	25.6±0.2	0.45	1099±7	121±1
	24	6.2±0.0	66.6±1.1	33.3±0.1	0.50	1815±22	199±2
AgNWs@IONCs@PEI	12	4.1±0.4	31.6±2.0	13.9±0.7	0.44	503±49	55±5
	16	5.9±0.2	42.3±2.2	21.7±0.7	0.51	1019±67	111±7
	24	9.5±0.2	47.6±1.6	32.1±1.7	0.67	2103±113	231±12
200 kHz							
IONCs@COOH	12	3.5±0.0	61.4±0.1	25.7±0.1	0.42	900±8	179±2
	16	4.2±0.0	71.0±0.6	30.8±0.3	0.43	1286±13	256±3
	24	5.4±0.0	78.9±1.1	37.1±0.5	0.47	1962±51	391±10
IONCs@PEI	12	4.0±0.1	44.5±0.2	20.1±0.5	0.45	720±21	143±4
	16	4.9±0.0	55.4±0.4	25.4±0.1	0.46	1114±1	222±0
	24	6.7±0.0	65.1±0.8	33.4±0.3	0.51	1889±32	377±6
AgNWs@IONCs@PEI	12	4.5±0.4	30.0±1.3	13.7±2.0	0.46	516±87	103±17
	16	6.8±0.1	35.5±1.3	21.1±0.4	0.59	1006±30	200±6
	24	11.2±0.1	41.8±2.0	33.0±0.4	0.79	2229±58	444±12
300 kHz							
IONCs@COOH	12	3.7±0.0	58.2±0.5	25.1±0.1	0.43	901±9	271±3
	16	4.3±0.0	67.3±0.7	29.1±0.3	0.43	1219±13	367±4
	24	5.8±0.0	74.2±0.6	36.7±0.4	0.49	1960±21	589±6
IONCs@PEI	12	4.1±0.1	42.0±0.6	18.5±0.7	0.44	680±31	205±9
	16	5.1±0.0	52.6±0.4	24.6±0.4	0.47	1093±67	329±8
	24	7.2±0.2	61.8±0.4	33.1±1.2	0.54	1906±93	573±28
AgNWs@IONCs@PEI	12	5.4±0.3	27.4±1.3	15.6±1.2	0.57	599±41	180±12
	16	7.1±0.8	35.2±2.8	20.9±2.1	0.59	1034±121	311±37
	24	13.1±0.8	36.9±1.5	34.1±1.1	0.92	2245±38	675±11

The magnetization curve of the IONCs@COOH, IONCs@PEI, and AgNWs@IONCs@PEI samples are given in Figure 5.10. For all samples, a non-saturated hysteresis loop was observed at 12 and 16 kA.m^{-1} magnetic fields independent of the frequency of the field being applied. However, hysteresis loops reached saturation when the magnetic field strength was increased to 24 kA.m^{-1}. It has been reported that a higher H_{AC} field was required to achieve saturation magnetization.[77] Also, it was observed that the PEI conjugation on the IONCs@COOH sample slightly lowered the magnetization curve area. This reduction could be attributed to the increase in the hydrodynamic size of the IONCs@PEI sample, which affects the relaxation mode of nanoparticles.[78] Comparing the hysteresis loop responses of IONCs@PEI and AgNW@IONCs@PEI samples against the applied H_{AC} under varying frequencies, it was observed that the field under the loop was smaller than that of IONCs@PEI at 12 kA.m^{-1}. When the H_{AC} was increased to 16 kA.m^{-1}, the areas under the hysteresis loops of IONCs@PEI and AgNW@IONCs@PEI became closer together, and when the H_{AC} was increased further to 24 kA.m^{-1}, the field under the loop became more significant for AgNW@IONCs@PEI.

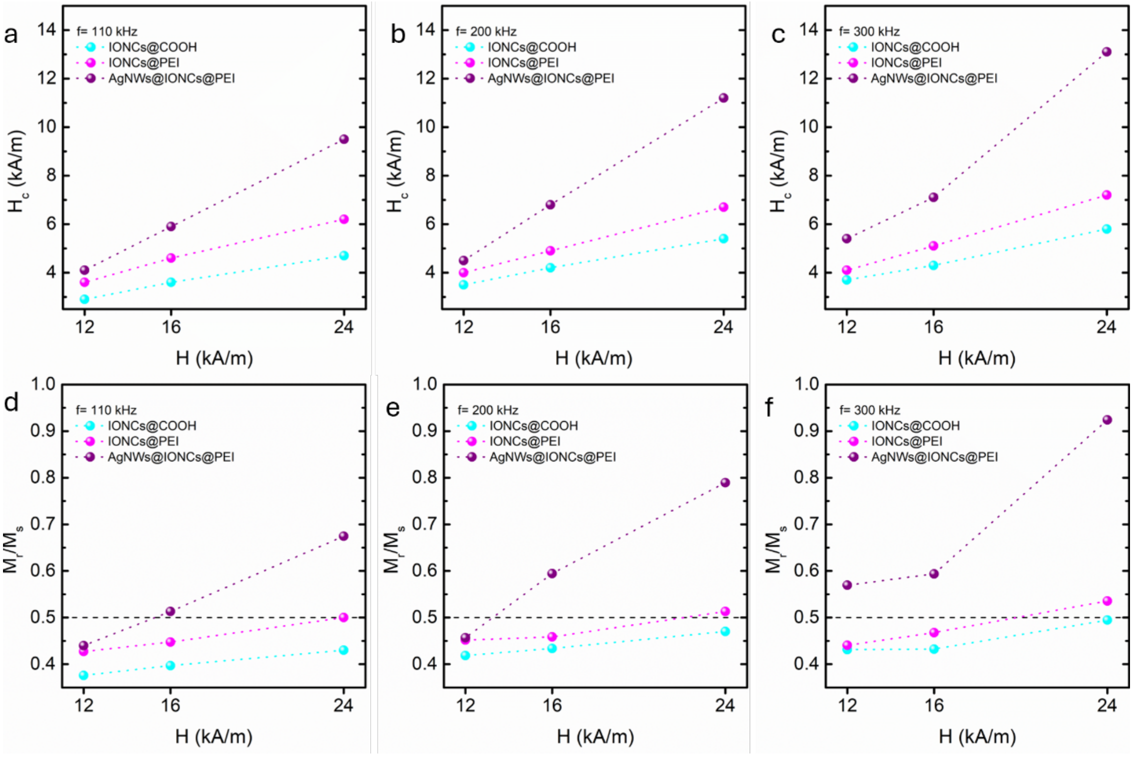

Figure 5.11. Evaluation of H_c (a-c) and M_s/M_r (d-f) values as a function applied magnetic field strength at various frequencies.

In order to understand the reason for the increase in magnetic loss observed in the AgNW@IONCs@PEI sample with an increasing magnetic field, the H_c, M_s, M_r, and M_r/M_s values extracted from the hysteresis loop were evaluated (Table 5.1). For all samples, the M_s value decreases with the increased field frequency; this could be attributed to the delay in the magnetization response to the applied AC field.[79] The M_s value was higher in IONCs@PEI nanoparticles than in AgNWs@IONCs@PEI for all examined magnetic field parameters. The imperfectly aligned chain-like structures could cause this behaviour. The magnetic moments of neighboring nanoparticles can be aligned antiparallel, resulting in a decrease in the net magnetization of the system. In addition, the magnetic anisotropy in these structures can create a preferred magnetization direction and limit the ability of nanoparticles to align their magnetic moments in the direction of the applied magnetic field, resulting in a lower saturation magnetization. However, as the applied magnetic field increased, the H_c value of the AgNWs@IONCs@PEI sample significantly increased, resulting in a larger hysteresis loop area. It was reported by Barrera et al. that strong dipolar interactions between nanoparticles, like in a chain configuration, can increase the overall energy barrier, making the coercive field much larger than the vertex field (Figure 5.11 a-c).[80]

Another essential characteristic of the hysteresis loops that provides details on the interactions of the magnetic particles is reduced remanent magnetization M_r/M_s. Figure 5.11 d-f shows the graphs of M_s/M_r values at various frequencies depending on the applied magnetic field intensity. The ratio of M_r/M_s equals 0.5 for a system of single-domain particles that do not interact with each other, according to the Stoner-Wohlfarth model.[77] Any deviation from this ratio provides information about particle interactions. If this ratio is less than 0.5, the decrease may be attributed to the dipolar interactions of randomly oriented nanoparticles; on the other hand, if the ratio is greater than 0.5, magnetic coupling may be indicated, as in the case of chain arrangement. It was observed that by increasing the applied H_{AC} to 24 kA.m^{-1}, the M_r/M_s values of the AgNWs@IONCs@PEI reached 0.67, 0.79, and 0.92 for frequencies of 110, 200, and 300 kHz, respectively, whereas the M_r/M_s value of the IONCs@PEI sample was around 0.50 for the same magnetic field conditions.

Figure 5.12 shows that the SAR values of IONCs@COOH, IONCs@PEI, and AgNWs@IONCs@PEI increase with increasing frequency and magnetic field. The dependence of SAR value on f and H_{AC} has been shown in literature theoretically and experimentally.[81,82] In Figure 5.12, the area of the hysteresis curve was increased with increasing H_{AC}, and the highest SAR value was obtained at 300 kHz and 24 kA.m^{-1} for all samples, as expected. Generally, the SAR value is proportional to the square of the H_{AC}. The effect of frequency is more complex than H_{AC}. In general, hysteresis losses increase with increasing frequency because, at higher frequencies, the magnetic domains have less time to reorient themselves in response to the changing magnetic field. As a result, more energy is dissipated as heat. For the H_{AC} values of 12 and 16 kA.m^{-1}, the SAR values of IONCs@PEI were 121 and 222 W/g, while the corresponding SAR values for AgNWs@IONCs@PEI were 112 and 200 W/g, respectively. It is worth noting that the AgNWs@IONCs@PEI sample has the highest SAR value when a field of 24 kA.m^{-1} is applied throughout all the frequencies.

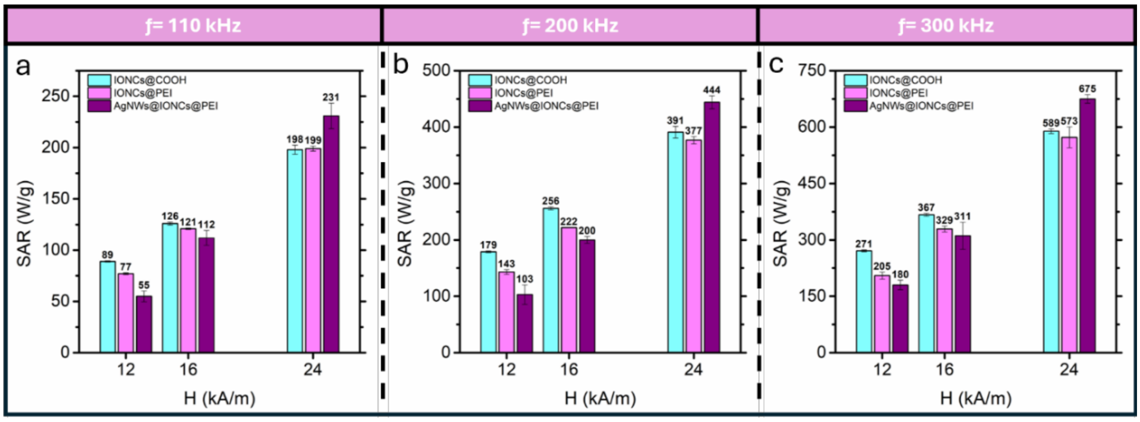

Figure 5.12. The SAR values of IONCs@COOH, IONCs@PEI, and AgNWs@IONCs@PEI under various magnetic field strengths and frequencies of 110 (a), 200 (b), and 300 kHz (c).

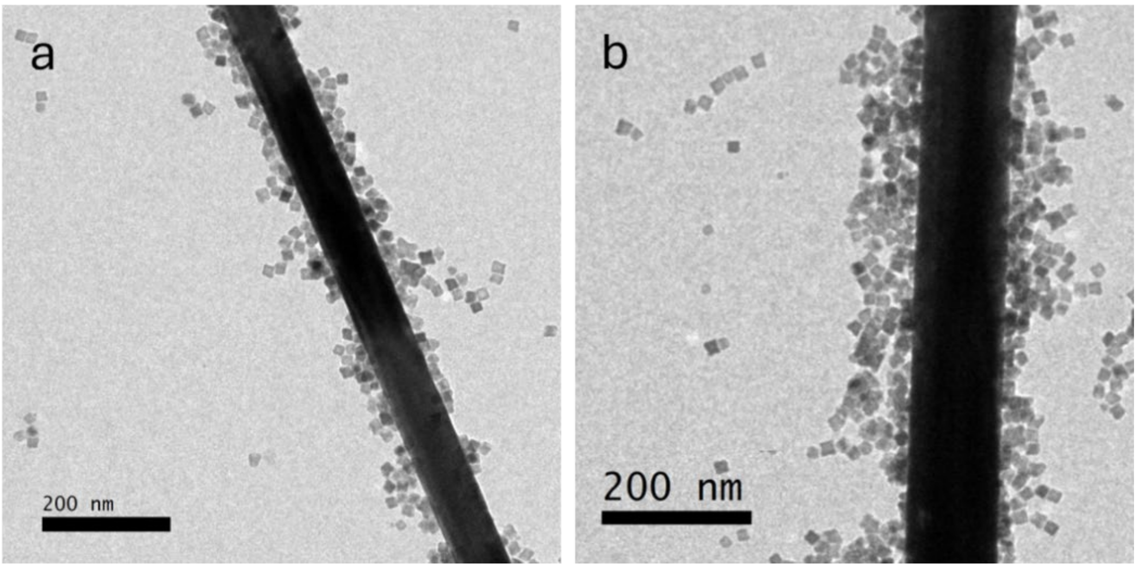

Figure 5.13. TEM images of the AgNWs@IONCs@PEI specimen after AC magnetometer measurement.

The strength of magnetic dipolar coupling depends on the distance between magnetic nanoparticles and the applied magnetic field strength. Low magnetic field strengths may not be sufficient to form stable chain-like structures, and the nanoparticles may remain randomly dispersed. Under higher field strengths, dipolar interactions become stronger and promote the formation of chain-like structures. The magnetic moments of the nanoparticles align with the field, and the dipolar forces between them pull the particles together into chains or columns. It can be concluded that the magnetic nanoparticles in the AgNWs@IONCs@PEI sample are arranged anisotropically in chains or columns at 24 kA.m^{-1}, the arising dipolar interactions increase the uniaxial anisotropy, leading to collective magnetization behavior and resulting in the formation of a higher coercive field[81]. The H_{AC}-dependent chain formation explains the high SAR values obtained under 24 kA.m^{-1} magnetic field intensity in the AgNWs@IONCs@PEI sample. According to Morales et al., the larger the H_{AC}, the more pronounced the chain formation is by many chains or long chains.[77] The anisotropic arrangement of magnetic nanoparticles resulted in a higher coercive field and a higher SAR value in the presented study.

In addition, TEM analysis was performed on the AgNWs@IONCs@PEI sample after the AC magnetometer measurements, and the images were given in Figure 5.13. It can be concluded that IONCs were successfully immobilized on the surface of AgNWs. Thus, the assemblies on the template were largely preserved even after AC magnetometer measurements.

5.4. Conclusion

IONCs were successfully assembled into chain-like structures by decorating the surfaces of AgNWs. The high aspect ratio of AgNWs enables long-range ordering of IONCs. The heating efficiency of the nanostructures was analyzed by AC magnetometers, and SAR values were calculated using instrument software. The results showed that the AgNWs@IONCs@PEI sample had the highest SAR values when the applied magnetic field strength was increased to 24 kA.m^{-1}, regardless of the field frequency. The data of M_s, H_c, and M_r/Ms extracted from the dynamic hysteresis loop indicates that the dipole coupling of the magnetic moments can be promoted at 24 kA.m^{-1} under these experimental conditions. Lower fields (i.e., 12 and 16 kA.m^{-1}) were insufficient to excite the chain-like structure for AgNWs@IONCs@PEI, leading to lower SAR values, most likely due to the antiparallel alignment of the magnetic moments of the nanoparticles. Also, due to the immobilization of IONCs on AgNWs, the chain-like structures were retained when the magnetic field was removed.

CHAPTER 6

CONCLUSION AND FUTURE DIRECTIONS

This thesis highlights the synthesis, characterization, and applications of silver nanowires and superparamagnetic iron oxide nanocubes, focusing on their functionalization and hybridization for magnetic hyperthermia applications.

High-quality AgNWs were synthesized using an environmentally friendly glycerol-water mixture in the open atmosphere via polyol synthesis. First, optimum values for temperature, PVP-to-AgNO$_3$ mole ratio, and promoter amount were determined using a single transition metal salt. Then, by keeping these experimental conditions constant, the effects of various metal salts (i.e., CuCl$_2$, MnCl$_2$, FeCl$_3$, CoCl$_2$, CrCl$_3$, and ZnCl$_2$) on the morphology were investigated. It was shown that transition metal salts significantly affected the morphology of AgNWs. The salts promote the one-dimensional growth of silver nanoparticles by removing oxygen from the silver seed surfaces. Furthermore, the reaction time and mixing conditions were optimized to determine the optimum conditions to produce high aspect ratio AgNWs, and when CuCl$_2$ was used as a promoter, 400 AgNWs were obtained.

IONCs were successfully assembled onto the surfaces of AgNWs as chain-like structures to enhance magnetic anisotropy. IONCs were synthesized using the solvothermal method, and their surfaces were modified with PEI to decorate them on AgNWs mainly via electrostatic attraction interactions. The high aspect ratio of AgNWs enabled the long-range organization of IONCs, forming stable chain-like assemblies. Magnetic characterization of the samples was carried out using an AC magnetometer. SAR values showed that AgNWs@IONCs@PEI structures achieved the highest SAR at 24 kA.m^{-1} magnetic field strength, independent of the field frequency. Magnetization data (M$_s$, H$_c$, and M$_r$/M$_s$) obtained from dynamic hysteresis loops indicate that the dipole coupling of magnetic moments increases at this field strength. At lower field strengths (12 and 16 kA.m^{-1}), insufficient excitation limited the SAR values, probably due to the antiparallel alignment of magnetic moments. Additionally, due to the immobilization of IONCs on AgNWs, the chain-like structures were preserved after removing the magnetic field.

This work has provided a pathway for the environmentally friendly synthesis of silver nanowires and their innovative use in magnetic nanostructure assemblies. Future work can focus on improving green synthesis parameters by exploring other environmentally friendly solvents and stabilizers. The scalability of the synthesis can be addressed to advance green synthesis methods toward commercial viability. Developing cost-effective, continuous-flow systems could enable the large-scale realization of green synthesis of AgNWs suitable for industrial applications.

Furthermore, AgNWs@IONCs assemblies have shown promising SAR values for magnetic hyperthermia. Future research can examine their behavior in biological environments, including in vivo studies, to evaluate their therapeutic efficacy, biocompatibility, and stability. Based on the chain-like assembly of IONCs on AgNWs templates, further structural modifications can be explored to maximize magnetic dipole coupling and SAR values. For instance, examining the effects of varying IONCs sizes, interparticle distances, and surface functionalizing groups can lead to structures with optimized heating efficiency under different field strengths. In addition, the AgNW@IONCs hybrid structure can be a versatile platform for various applications. By incorporating other materials, such as conductive polymers or carbon-based materials, these hybrid structures can be developed for various applications such as catalysis, energy storage, and sensing.

REFERENCES

1. Hemmati, S.; Harris, M. T.; Barkey, D. P. Polyol Silver Nanowire Synthesis and the Outlook for a Green Process. *J Nanomater* **2020**, *2020*. https://doi.org/10.1155/2020/9341983.
2. Sun, Y.; Mayers, B.; Herricks, T.; Xia, Y. Polyol Synthesis of Uniform Silver Nanowires: A Plausible Growth Mechanism and the Supporting Evidence. *Nano Lett* **2003**, *3* (7), 955–960. https://doi.org/10.1021/nl034312m.
3. Sun, Y. Silver Nanowires – Unique Templates for Functional Nanostructures. *Nanoscale* **2010**, *2* (9), 1626. https://doi.org/10.1039/c0nr00258e.
4. Gavilán, H.; Rizzo, G. M. R.; Silvestri, N.; Mai, B. T.; Pellegrino, T. Scale-up Approach for the Preparation of Magnetic Ferrite Nanocubes and Other Shapes with Benchmark Performance for Magnetic Hyperthermia Applications. *Nat Protoc* **2023**, *18* (3), 783–809. https://doi.org/10.1038/s41596-022-00779-3.
5. Gavilán, H.; Simeonidis, K.; Myrovali, E.; Mazarío, E.; Chubykalo-Fesenko, O.; Chantrell, R.; Balcells, Ll.; Angelakeris, M.; Morales, M. P.; Serantes, D. How Size, Shape and Assembly of Magnetic Nanoparticles Give Rise to Different Hyperthermia Scenarios. *Nanoscale* **2021**, *13* (37), 15631–15646. https://doi.org/10.1039/D1NR03484G.
6. Rajan, A.; Sahu, N. K. Review on Magnetic Nanoparticle-Mediated Hyperthermia for Cancer Therapy. *Journal of Nanoparticle Research* **2020**, *22* (11), 319. https://doi.org/10.1007/s11051-020-05045-9.
7. Ovejero, J. G.; Spizzo, F.; Morales, M. P.; Del Bianco, L. Nanoparticles for Magnetic Heating: When Two (or More) Is Better Than One. *Materials* **2021**, *14* (21), 6416. https://doi.org/10.3390/ma14216416.
8. Rónavári, A.; Igaz, N.; Adamecz, D. I.; Szerencsés, B.; Molnar, C.; Kónya, Z.; Pfeiffer, I.; Kiricsi, M. Green Silver and Gold Nanoparticles: Biological Synthesis Approaches and Potentials for Biomedical Applications. *Molecules* **2021**, *26* (4), 844. https://doi.org /10.3390/molecules26040844.
9. Nguyen, Q. N.; Wang, C.; Shang, Y.; Janssen, A.; Xia, Y. Colloidal Synthesis of Metal Nanocrystals: From Asymmetrical Growth to Symmetry Breaking. *Chem Rev* **2023**, *123* (7), 3693–3760. https://doi.org/10.1021/acs.chemrev.2c00468.

10. Lee, S.; Jun, B.-H. Silver Nanoparticles: Synthesis and Application for Nanomedicine. *Int J Mol Sci* **2019**, *20* (4), 865. https://doi.org/10.3390/ijms20040865.
11. Zhang, Z.; Shen, W.; Xue, J.; Liu, Y.; Liu, Y.; Yan, P.; Liu, J.; Tang, J. Recent Advances in Synthetic Methods and Applications of Silver Nanostructures. *Nanoscale Res Lett* **2018**, *13* (1), 54. https://doi.org/10.1186/s11671-018-2450-4.
12. Wiley, B.; Sun, Y.; Xia, Y. Synthesis of Silver Nanostructures with Controlled Shapes and Properties. *Acc Chem Res* **2007**, *40* (10), 1067–1076. https://doi.org/10.1021/ar7000974.
13. Zhang, P.; Wyman, I.; Hu, J.; Lin, S.; Zhong, Z.; Tu, Y.; Huang, Z.; Wei, Y. Silver Nanowires: Synthesis Technologies, Growth Mechanism and Multifunctional Applications. *Materials Science and Engineering: B* **2017**, *223*, 1–23. https://doi.org/10.1016/j.mseb.2017.05.002.
14. Jones, R. S.; Draheim, R. R.; Roldo, M. Silver Nanowires: Synthesis, Antibacterial Activity and Biomedical Applications. *Applied Sciences* **2018**, *8* (5), 673. https://doi.org/10.3390/app8050673.
15. Kwon, J.; Suh, Y. D.; Lee, J.; Lee, P.; Han, S.; Hong, S.; Yeo, J.; Lee, H.; Ko, S. H. Recent Progress in Silver Nanowire Based Flexible/Wearable Optoelectronics. *J Mater Chem C Mater* **2018**, *6* (28), 7445–7461. https://doi.org/10.1039/C8TC01024B
16. Jung, J.; Cho, H.; Yuksel, R.; Kim, D.; Lee, H.; Kwon, J.; Lee, P.; Yeo, J.; Hong, S.; Unalan, H. E.; Han, S.; Ko, S. H. Stretchable/Flexible Silver Nanowire Electrodes for Energy Device Applications. *Nanoscale* **2019**, *11* (43), 20356–20378. https://doi.org/10.1039/C9NR04193A.
17. Singh, M.; Movia, D.; Mahfoud, O. K.; Volkov, Y.; Prina-Mello, A. Silver Nanowires as Prospective Carriers for Drug Delivery in Cancer Treatment: An in Vitro Biocompatibility Study on Lung Adenocarcinoma Cells and Fibroblasts. *Eur J Nanomed* **2013**, *5* (4), 195–204. https://doi.org/10.1515/ejnm-2013-0024.
18. Zhang, P.; Wyman, I.; Hu, J.; Lin, S.; Zhong, Z.; Tu, Y.; Huang, Z.; Wei, Y. Silver Nanowires: Synthesis Technologies, Growth Mechanism and Multifunctional Applications. *Materials Science and Engineering: B* **2017**, *223*, 1–23. https://doi.org/https://doi.org/10.1016/j.mseb.2017.05.002.

19. Kumar, A.; Shaikh, M. O.; Chuang, C.-H. Silver Nanowire Synthesis and Strategies for Fabricating Transparent Conducting Electrodes. *Nanomaterials* **2021**, *11* (3), 693. https://doi.org/10.3390/nano11030693.
20. Yang, Z.; Qian, H.; Chen, H.; Anker, J. N. One-Pot Hydrothermal Synthesis of Silver Nanowires via Citrate Reduction. *J Colloid Interface Sci* **2010**, *352* (2), 285–291. https://doi.org/10.1016/j.jcis.2010.08.072.
21. Wang, Z.; Liu, J.; Chen, X.; Wan, J.; Qian, Y. A Simple Hydrothermal Route to Large-Scale Synthesis of Uniform Silver Nanowires. *Chemistry – A European Journal* **2005**, *11* (1), 160–163. https://doi.org/10.1002/chem.200400705.
22. Sun, Y.; Mayers, B.; Herricks, T.; Xia, Y. Polyol Synthesis of Uniform Silver Nanowires: A Plausible Growth Mechanism and the Supporting Evidence. *Nano Lett* **2003**, *3* (7), 955–960. https://doi.org/10.1021/nl034312m.
23. Jia, C.; Yang, P.; Zhang, A. Glycerol and Ethylene Glycol Co-Mediated Synthesis of Uniform Multiple Crystalline Silver Nanowires. *Mater Chem Phys* **2014**, *143* (2), 794–800. https://doi.org/10.1016/j.matchemphys.2013.10.015.
24. Skrabalak, S. E.; Wiley, B. J.; Kim, M.; Formo, E. V.; Xia, Y. On the Polyol Synthesis of Silver Nanostructures: Glycolaldehyde as a Reducing Agent. *Nano Lett* **2008**, *8* (7), 2077–2081. https://doi.org/10.1021/nl800910d.
25. Wiley, B.; Sun, Y.; Xia, Y. Polyol Synthesis of Silver Nanostructures: Control of Product Morphology with Fe(II) or Fe(III) Species. *Langmuir* **2005**, *21* (18), 8077–8080. https://doi.org/10.1021/la050887i.
26. Sun, Y.; Mayers, B.; Herricks, T.; Xia, Y. Polyol Synthesis of Uniform Silver Nanowires: A Plausible Growth Mechanism and the Supporting Evidence. *Nano Lett* **2003**, *3* (7), 955–960. https://doi.org/10.1021/nl034312m.
27. Liu, X.; Zhang, F.; Huang, R.; Pan, C.; Zhu, J. Capping Modes in PVP-Directed Silver Nanocrystal Growth: Multi-Twinned Nanorods versus Single-Crystalline Nano-Hexapods. *Cryst Growth Des* **2008**, *8* (6), 1916–1923. https://doi.org/10.1021/cg701128b.
28. Jiang, P.; Li, S.; Xie, S.; Gao, Y.; Song, L. Machinable Long PVP-Stabilized Silver Nanowires. *Chemistry – A European Journal* **2004**, *10* (19), 4817–4821. https://doi.org/10.1002/chem.200400318.
29. Zhu, J.-J.; Kan, C.-X.; Wan, J.-G.; Han, M.; Wang, G.-H. High-Yield Synthesis of Uniform Ag Nanowires with High Aspect Ratios by Introducing the Long-Chain

PVP in an Improved Polyol Process. *J Nanomater* **2011**, *2011*, 1–7. https://doi.org/10.1155/2011/982547.

30. Coskun, S.; Aksoy, B.; Unalan, H. E. Polyol Synthesis of Silver Nanowires: An Extensive Parametric Study. *Cryst Growth Des* **2011**, *11* (11), 4963–4969. https://doi.org/10.1021/cg200874g.
31. Prabukumar, C.; Bhat, K. U. Beneficial Effect of Manganese(II) Ions on the Morphology of Polyol Synthesised Silver Nanowires. *Electronic Materials Letters* **2020**, *16* (3), 264–275. https://doi.org/10.1007/s13391-020-00211-6.
32. Chen, T.; Wang, H.; Yang, H.; Bai, S.; Guo, X. Mixed Polyols Synthesis of High Aspect Ratio Silver Nanowires for Transparent Conductive Films. *Mater Res Express* **2018**, *5* (6), 066426. https://doi.org/10.1088/2053-1591/aacd3e.
33. Gómez-Acosta, A.; Manzano-Ramírez, A.; López-Naranjo, E. J.; Apatiga, L. M.; Herrera-Basurto, R.; Rivera-Muñoz, E. M. Silver Nanostructure Dependence on the Stirring-Time in a High-Yield Polyol Synthesis Using a Short-Chain PVP. *Mater Lett* **2015**, *138*, 167–170. https://doi.org/10.1016/j.matlet.2014.09.109.
34. Bergin, S. M.; Chen, Y.-H.; Rathmell, A. R.; Charbonneau, P.; Li, Z.-Y.; Wiley, B. J. The Effect of Nanowire Length and Diameter on the Properties of Transparent, Conducting Nanowire Films. *Nanoscale* **2012**, *4* (6), 1996. https://doi.org/10.1039/c2nr30126a.
35. Zhang, Y.; Wang, J.; Yang, P. Convenient Synthesis of Ag Nanowires with Tunable Length and Morphology. *Mater Res Bull* **2013**, *48* (2), 461–468. https://doi.org/10.1016/j.materresbull.2012.11.011.
36. Zeng, X.; Zhou, B.; Gao, Y.; Wang, C.; Li, S.; Yeung, C. Y.; Wen, W. J. Structural Dependence of Silver Nanowires on Polyvinyl Pyrrolidone (PVP) Chain Length. *Nanotechnology* **2014**, *25* (49). https://doi.org/10.1088/0957-4484/25/49/495601.
37. Dennis, C. L.; Ivkov, R. Physics of Heat Generation Using Magnetic Nanoparticles for Hyperthermia. *International Journal of Hyperthermia* **2013**, *29* (8), 715–729. https://doi.org/10.3109/02656736.2013.836758.
38. Mody, V. V.; Singh, A.; Wesley, B. Basics of Magnetic Nanoparticles for Their Application in the Field of Magnetic Fluid Hyperthermia. *Eur J Nanomed* **2013**, *5* (1). https://doi.org/10.1515/ejnm-2012-0008.
39. Estelrich, J.; Escribano, E.; Queralt, J.; Busquets, M. Iron Oxide Nanoparticles for Magnetically-Guided and Magnetically-Responsive Drug Delivery. *Int J Mol Sci* **2015**, *16* (4), 8070–8101. https://doi.org/10.3390/ijms16048070.

40. Giustini, A. J.; Petryk, A. A.; Cassim, S. M.; Tate, J. A.; Baker, I.; Hoopes, P. J. Magnetic Nanoparticle Hyperthermia In Cancer Treatment. *Nano Life* **2010**, *01* (01n02), 17–32. https://doi.org/10.1142/S1793984410000067.

41. Deatsch, A. E.; Evans, E. E. Heating Efficiency in Magnetic Nanoparticle Hyperthermia. *J Magn Magn Mater* **2014**, *354*, 163–172. https://doi.org/10.1016/j.jmmm.2013.11.006.

42. Ma, Z.; Mohapatra, J.; Wei, K.; Liu, J. P.; Sun, S. Magnetic Nanoparticles: Synthesis, Anisotropy, and Applications. *Chem Rev* **2023**, *123* (7), 3904–3943. https://doi.org/10.1021/acs.chemrev.1c00860.

43. Alipour, A.; Soran-Erdem, Z.; Utkur, M.; Sharma, V. K.; Algin, O.; Saritas, E. U.; Demir, H. V. A New Class of Cubic SPIONs as a Dual-Mode T1 and T2 Contrast Agent for MRI. *Magn Reson Imaging* **2018**, *49*, 16–24. https://doi.org/10.1016/j.mri.2017.09.013.

44. Scialabba, C.; Puleio, R.; Peddis, D.; Varvaro, G.; Calandra, P.; Cassata, G.; Cicero, L.; Licciardi, M.; Giammona, G. Folate Targeted Coated SPIONs as Efficient Tool for MRI. *Nano Res* **2017**, *10* (9), 3212–3227. https://doi.org/10.1007/s12274-017-1540-4.

45. Gavilán, H.; Avugadda, S. K.; Fernández-Cabada, T.; Soni, N.; Cassani, M.; Mai, B. T.; Chantrell, R.; Pellegrino, T. Magnetic Nanoparticles and Clusters for Magnetic Hyperthermia: Optimizing Their Heat Performance and Developing Combinatorial Therapies to Tackle Cancer. *Chem Soc Rev* **2021**, *50* (20), 11614–11667. https://doi.org/10.1039/D1CS00427A.

46. Gavilán, H.; Simeonidis, K.; Myrovali, E.; Mazarío, E.; Chubykalo-Fesenko, O.; Chantrell, R.; Balcells, Ll.; Angelakeris, M.; Morales, M. P.; Serantes, D. How Size, Shape and Assembly of Magnetic Nanoparticles Give Rise to Different Hyperthermia Scenarios. *Nanoscale* **2021**, *13* (37), 15631–15646. https://doi.org/10.1039/D1NR03484G.

47. Silvestri, N.; Gavilán, H.; Guardia, P.; Brescia, R.; Fernandes, S.; Samia, A. C. S.; Teran, F. J.; Pellegrino, T. Di- and Tri-Component Spinel Ferrite Nanocubes: Synthesis and Their Comparative Characterization for Theranostic Applications. *Nanoscale* **2021**, *13* (32), 13665–13680. https://doi.org/10.1039/D1NR01044A.

48. Chugh, V. K.; Liang, S.; Tonini, D.; Saha, R.; Liu, J.; Yari, P.; D. Krishna, V.; Cheeran, M. C.-J.; Wu, K.; Wang, J.-P. Static and Dynamic Magnetization Responses of Self-Assembled Magnetic Nanoparticle Chains. *The Journal of*

Physical Chemistry C **2023**, *127* (37), 18494–18505. https://doi.org/10.1021/acs.jpcc.3c03755.

49. Morales, I.; Costo, R.; Mille, N.; Carrey, J.; Hernando, A.; de la Presa, P. Time-Dependent AC Magnetometry and Chain Formation in Magnetite: The Influence of Particle Size, Initial Temperature and the Shortening of the Relaxation Time by the Applied Field. *Nanoscale Adv* **2021**, *3* (20), 5801–5812. https://doi.org/10.1039/D1NA00463H.
50. Myrovali, E.; Papadopoulos, K.; Iglesias, I.; Spasova, M.; Farle, M.; Wiedwald, U.; Angelakeris, M. Long-Range Ordering Effects in Magnetic Nanoparticles. *ACS Appl Mater Interfaces* **2021**, *13* (18), 21602–21612. https://doi.org/10.1021/acsami.1c01820.
51. Niculaes, D.; Lak, A.; Anyfantis, G. C.; Marras, S.; Laslett, O.; Avugadda, S. K.; Cassani, M.; Serantes, D.; Hovorka, O.; Chantrell, R.; Pellegrino, T. Asymmetric Assembling of Iron Oxide Nanocubes for Improving Magnetic Hyperthermia Performance. *ACS Nano* **2017**, *11* (12), 12121–12133. https://doi.org/10.1021/acsnano.7b05182.
52. Gavilán, H.; Rizzo, G. M. R.; Silvestri, N.; Mai, B. T.; Pellegrino, T. Scale-up Approach for the Preparation of Magnetic Ferrite Nanocubes and Other Shapes with Benchmark Performance for Magnetic Hyperthermia Applications. *Nat Protoc* **2023**, *18* (3), 783–809. https://doi.org/10.1038/s41596-022-00779-3.
53. Guardia, P.; Riedinger, A.; Kakwere, H.; Gazeau, F.; Pellegrino, T. Magnetic Nanoparticles for Magnetic Hyperthermia and Controlled Drug Delivery. In *Bio- and Bioinspired Nanomaterials*; Wiley, **2014**; pp 139–172. https://doi.org/10.1002/9783527675821.ch06.
54. Massart, R. Preparation of Aqueous Magnetic Liquids in Alkaline and Acidic Media. *IEEE Trans Magn* **1981**, *17* (2), 1247–1248. https://doi.org/10.1109/TMAG.1981.1061188.
55. Guardia, P.; Riedinger, A.; Nitti, S.; Pugliese, G.; Marras, S.; Genovese, A.; Materia, M. E.; Lefevre, C.; Manna, L.; Pellegrino, T. One Pot Synthesis of Monodisperse Water Soluble Iron Oxide Nanocrystals with High Values of the Specific Absorption Rate. *J Mater Chem B* **2014**, *2* (28), 4426. https://doi.org/10.1039/c4tb00061g.
56. Gavilán, H.; Rizzo, G. M. R.; Silvestri, N.; Mai, B. T.; Pellegrino, T. Scale-up Approach for the Preparation of Magnetic Ferrite Nanocubes and Other Shapes

with Benchmark Performance for Magnetic Hyperthermia Applications. *Nat Protoc* **2023**, *18* (3), 783–809. https://doi.org/10.1038/s41596-022-00779-3.

57. Lin, L.; Bi, X.; Gu, Y.; Wang, F.; Ye, J. Surface-Enhanced Raman Scattering Nanotags for Bioimaging. *J Appl Phys* **2021**, *129* (19). https://doi.org/10.1063/5.0047578.
58. Hamans, R. F.; Parente, M.; Garcia-Etxarri, A.; Baldi, A. Optical Properties of Colloidal Silver Nanowires. *The Journal of Physical Chemistry C* **2022**, *126* (20), 8703–8709. https://doi.org/10.1021/acs.jpcc.2c01251.
59. Kim, H.-A.; Seo, J.-K.; Kim, T.; Lee, B.-T. Nanometrology and Its Perspectives in Environmental Research. *Environ Health Toxicol* **2014**, *29*, e2014016. https://doi.org/10.5620/eht.e2014016.
60. Madeira, A.; Papanastasiou, D. T.; Toupance, T.; Servant, L.; Tréguer-Delapierre, M.; Bellet, D.; Goldthorpe, I. A. Rapid Synthesis of Ultra-Long Silver Nanowires for High Performance Transparent Electrodes. *Nanoscale Adv* **2020**, *2* (9), 3804–3808. https://doi.org/10.1039/D0NA00392A.
61. Parente, M.; van Helvert, M.; Hamans, R. F.; Verbroekken, R.; Sinha, R.; Bieberle-Hütter, A.; Baldi, A. Simple and Fast High-Yield Synthesis of Silver Nanowires. *Nano Lett* **2020**, *20* (8), 5759–5764. https://doi.org/10.1021/acs.nanolett.0c01565.
62. Gebeyehu, M. B.; Chala, T. F.; Chang, S.-Y.; Wu, C.-M.; Lee, J.-Y. Synthesis and Highly Effective Purification of Silver Nanowires to Enhance Transmittance at Low Sheet Resistance with Simple Polyol and Scalable Selective Precipitation Method. *RSC Adv* **2017**, *7* (26), 16139–16148. https://doi.org/10.1039/C7RA00238F.
63. Bari, B.; Lee, J.; Jang, T.; Won, P.; Ko, S. H.; Alamgir, K.; Arshad, M.; Guo, L. J. Simple Hydrothermal Synthesis of Very-Long and Thin Silver Nanowires and Their Application in High Quality Transparent Electrodes. *J Mater Chem A Mater* **2016**, *4* (29), 11365–11371. https://doi.org/10.1039/C6TA03308C.
64. Fievet, F.; Lagier, J.; Blin, B.; Beaudoin, B.; Figlarz, M. Homogeneous and Heterogeneous Nucleations in the Polyol Process for the Preparation of Micron and Submicron Size Metal Particles. *Solid State Ion* **1989**, *32–33*, 198–205. https://doi.org/10.1016/0167-2738(89)90222-1.
65. Sun, Y.; Mayers, B.; Herricks, T.; Xia, Y. Polyol Synthesis of Uniform Silver Nanowires: A Plausible Growth Mechanism and the Supporting Evidence. *Nano Lett* **2003**, *3* (7), 955–960. https://doi.org/10.1021/nl034312m.

66. Fowles, J.; Banton, M.; Klapacz, J.; Shen, H. A Toxicological Review of the Ethylene Glycol Series: Commonalities and Differences in Toxicity and Modes of Action. *Toxicol Lett* **2017**, *278*, 66–83. https://doi.org/10.1016/j.toxlet.2017.06.009.

67. Trung, T. N.; Arepalli, V. K.; Gudala, R.; Kim, E.-T. Polyol Synthesis of Ultrathin and High-Aspect-Ratio Ag Nanowires for Transparent Conductive Films. *Mater Lett* **2017**, *194*, 66–69. https://doi.org/10.1016/j.matlet.2017.02.011.

68. Korte, K. E.; Skrabalak, S. E.; Xia, Y. Rapid Synthesis of Silver Nanowires through a CuCl- or $CuCl_2$ -Mediated Polyol Process. *J. Mater. Chem.* **2008**, *18* (4), 437–441. https://doi.org/10.1039/B714072J.

69. de Mongeot, F. B.; Cupolillo, A.; Valbusa, U.; Rocca, M. O2 Dissociation on Ag(001): The Role of Kink Sites. *Chem Phys Lett* **1997**, *270* (3–4), 345–350. https://doi.org/10.1016/S0009-2614(97)00381-3.

70. Nemati, Z.; Alonso, J.; Rodrigo, I.; Das, R.; Garaio, E.; García, J. Á.; Orue, I.; Phan, M.-H.; Srikanth, H. Improving the Heating Efficiency of Iron Oxide Nanoparticles by Tuning Their Shape and Size. *The Journal of Physical Chemistry C* **2018**, *122* (4), 2367–2381. https://doi.org/10.1021/acs.jpcc.7b10528.

71. Morales, I.; Costo, R.; Mille, N.; Da Silva, G. B.; Carrey, J.; Hernando, A.; De la Presa, P. High Frequency Hysteresis Losses on γ-Fe2O3 and Fe3O4: Susceptibility as a Magnetic Stamp for Chain Formation. *Nanomaterials* **2018**, *8* (12), 970. https://doi.org/10.3390/nano8120970.

72. Sun, Y. Silver Nanowires – Unique Templates for Functional Nanostructures. *Nanoscale* **2010**, *2* (9), 1626. https://doi.org/10.1039/c0nr00258e.

73. Sarisozen, S.; Tertemiz, N. A.; Arica, T. A.; Polat, N.; Kocabas, C.; Balci, F. M.; Balci, S. Transition Metal Salt Promoted, Green, and High-Yield Synthesis of Silver Nanowires for Flexible Transparent Conductive Electrodes. *ChemistrySelect* **2021**, *6* (44), 12548–12554. https://doi.org/10.1002/slct.202103434.

74. Chen, Z.; Lv, Z.; Sun, Y.; Chi, Z.; Qing, G. Recent Advancements in Polyethyleneimine-Based Materials and Their Biomedical, Biotechnology, and Biomaterial Applications. *J Mater Chem B* **2020**, *8* (15), 2951–2973. https://doi.org/10.1039/C9TB02271F.

75. Cruz-Acuña, M.; Maldonado-Camargo, L.; Dobson, J.; Rinaldi, C. From Oleic Acid-Capped Iron Oxide Nanoparticles to Polyethyleneimine-Coated Single-

Particle Magnetofectins. *Journal of Nanoparticle Research* **2016**, *18* (9), 268. https://doi.org/10.1007/s11051-016-3577-9.

76. Narayanasamy, K. K.; Cruz-Acuña, M.; Rinaldi, C.; Everett, J.; Dobson, J.; Telling, N. D. Alternating Current (AC) Susceptibility as a Particle-Focused Probe of Coating and Clustering Behaviour in Magnetic Nanoparticle Suspensions. *J Colloid Interface Sci* **2018**, *532*, 536–545. https://doi.org/10.1016/j.jcis.2018.08.014.
77. Morales, I.; Costo, R.; Mille, N.; Da Silva, G. B.; Carrey, J.; Hernando, A.; De la Presa, P. High Frequency Hysteresis Losses on γ-Fe2O3 and Fe3O4: Susceptibility as a Magnetic Stamp for Chain Formation. *Nanomaterials* **2018**, *8* (12), 970. https://doi.org/10.3390/nano8120970.
78. Avugadda, S. K.; Soni, N.; Rodrigues, E. M.; Persano, S.; Pellegrino, T. Protease-Mediated *T* ₁ Contrast Enhancement of Multilayered Magneto-Gadolinium Nanostructures for Imaging and Magnetic Hyperthermia. *ACS Appl Mater Interfaces* **2024**, *16* (6), 6743–6755. https://doi.org/10.1021/acsami.3c13914.
79. Yamaminami, T.; Ota, S.; Trisnanto, S. B.; Ishikawa, M.; Yamada, T.; Yoshida, T.; Enpuku, K.; Takemura, Y. Power Dissipation in Magnetic Nanoparticles Evaluated Using the AC Susceptibility of Their Linear and Nonlinear Responses. *J Magn Magn Mater* **2021**, *517*, 167401. https://doi.org/10.1016/j.jmmm.2020.167401.
80. Barrera, G.; Allia, P.; Tiberto, P. Dipolar Interactions among Magnetite Nanoparticles for Magnetic Hyperthermia: A Rate-Equation Approach. *Nanoscale* **2021**, *13* (7), 4103–4121. https://doi.org/10.1039/D0NR07397K.
81. Deatsch, A. E.; Evans, E. E. Heating Efficiency in Magnetic Nanoparticle Hyperthermia. *J Magn Magn Mater* **2014**, *354*, 163–172. https://doi.org/10.1016/j.jmmm.2013.11.006.
82. Myrovali, E.; Papadopoulos, K.; Iglesias, I.; Spasova, M.; Farle, M.; Wiedwald, U.; Angelakeris, M. Long-Range Ordering Effects in Magnetic Nanoparticles. *ACS Appl Mater Interfaces* **2021**, *13* (18), 21602–21612. https://doi.org/10.1021/acsami.1c01820.

VITA

EDUCATION

2018-2024	Doctor of Philosophy *Department of Material Science and Engineering* *Izmir Institute of Technology*
2014-2017	Master of Science *Department of Material Science and Engineering* *Anadolu University*
2009-2014	Bachelor of Science *Department of Material Science and Engineering* *Anadolu University*

WORK EXPERIENCE

2018-	Research Assistant *Department of Material Science and Engineering* *Izmir Institute of Technology*
2023-2024	Visiting Researcher *Nanomaterials for Biomedical Applications* *Italian Institute of Technology*
06.2015- 09.2015	Erasmus Summer Intern *Advanced Ceramic Materials Laboratory* *University of Padova*

PUBLICATIONS

Arica, T. A., Balci, F. M., Balci, S., & Arica, M. Y. (2022). Highly porous poly (o-phenylenediamine) loaded magnetic carboxymethyl cellulose hybrid beads for removal of two model textile dyes. Fibers and Polymers, 23(10), 2838-2854.

Sarisozen, S., Tertemiz, N.A., Arica, T. A., Polat, N., Kocabas, C., Mert Balci, F., Balci, S. (2021). Transition Metal Salt Promoted, Green, and High-Yield Synthesis of Silver Nanowires for Flexible Transparent Conductive Electrodes. ChemistrySelect, 44, 12548-12554.

Arica, T.A., Isık, T., Guner, T., Horzum, N. and Demir, M.M. (2021). Advances in Electrospun Fiber-Based Flexible Nanogenerators for Wearable Applications. Macromolecular Materials and Engineering, 306, 2100143.

Arica, T. A, Guzelgulgen, M., Arslan Yildiz, A., Demir, M.M. (2021). Electrospun GelMA fibers and p(HEMA) matrix composite for corneal tissue engineering. Materials Science and Engineering: C, 120, 111720.

Arica, T. A, Topcu, G., Pala, A., Demir, M.M. (2020). Experimental Apparatus for Simultaneous Measurement of Triboelectricity and Triboluminescence. Measurement, 107316.

Arica, T. A., Kuman, M., Gercel, O., Ayas, E. (2019). Poly (dopamine) grafted bio-silica composite with tetraethylenepentamine ligands for enhanced adsorption of pollutants. Chemical Engineering Research and Design, 141, 317-327.

Arica, T. A., Ayas, E., & Arica, M. Y. (2017). Magnetic MCM-41 silica particles grafted with poly (glycidylmethacrylate) brush: Modification and application for removal of direct dyes. Microporous and Mesoporous Materials, 243, 164–175.